Ocean Dynamics (2019) 69:1253–1271
https://doi.org/10.1007/s10236-019-01303-0

Role of interannual equatorial forcing on the subsurface temperature dipole in the Bay of Bengal during IOD and ENSO events

Saikat Pramanik[1] · Sourav Sil[1] · Samiran Mandal[1] · Dipanjan Dey[1,2] · Abhijit Shee[1]

Received: 26 February 2019 / Accepted: 23 August 2019 / Published online: 4 November 2019
© Springer-Verlag GmbH Germany, part of Springer Nature 2019

Abstract

Role of equatorial forcing on the thermocline variability in the Bay of Bengal (BoB) during positive and negative phases of the Indian Ocean Dipole (IOD) and El Niño Southern Oscillation (ENSO) was investigated using the Regional Ocean Modeling System (ROMS) simulations during 1988 to 2015. Two numerical experiments were carried out for (i) the Indian Ocean Model (IOM) with interannual open boundary conditions and (ii) the BoB Model (BoBM) with climatological boundary conditions. The first mode of Sea Surface Height Anomalies (SSHA) variability showed a west-east dipole nature in both IOM and altimetry observations around 11°N, which was absent in the BoBM. The vertical section of temperature along the same latitude showed a sharp subsurface temperature dipole with a core at ~ 100 m depth. The positive (negative) subsurface temperature anomalies were observed over the whole northeastern BoB during NIOD (PIOD) and LN (EN) composites due to stronger (weaker) second downwelling Kelvin Waves. During the negative phases of IOD and ENSO, the cyclonic eddy on the southwestern BoB strengthened due to intensified southward coastal current along the western BoB and local wind stress. The subsurface temperature dipole was at its peak during October–December (OND) with 1-month lag from IOD and was evident from the Argo observations and other reanalysis datasets as well. A new BoB dipole index (BDI) was defined as the normalized difference of 100-m temperature anomaly and found to be closely related to the frequency of cyclones and the surface chlorophyll-a concentration in the BoB.

Keywords Bay of Bengal · Thermocline · ROMS · Kelvin and Rossby waves · Argos · Chlorophyll-a · Cyclones

1 Introduction

The Bay of Bengal (BoB) is a unique tropical ocean basin on the northeast of the Indian Ocean (IO) with three sides bounded by land (Fig. 1). The seasonally reversing monsoonal winds (northeasterly winds during December to February and strong southwesterly winds during June to September) make oceanic features different from the other tropical oceans (McCreary et al. 1993; Durand et al. 2009; Schott et al. 2009). Also, a large amount of freshwater influx from rivers in the Indian subcontinent plays important roles in oceanic processes (Jana et al. 2015, 2018; Thadathil et al. 2002). The thermocline of this basin is very important as it determines the upper layer thermal structure to govern the Indian monsoon (Gordon et al. 2016; Girishkumar et al. 2017; Vinayachandran et al. 2018). It also plays a role in the upper ocean heat content, cyclogenesis, upwelling zones for fisheries (Ali et al. 2018; Krishnamurti et al. 2017; Li et al. 2018; Balaguru et al. 2014; Chacko 2017; Girishkumar et al. 2014; Mandal et al. 2018), and sound propagation in the sea (Siderius et al. 2007).

The variations of the thermocline structure depend on the surface and sub-surface circulations. The seasonal variations of circulation and upper ocean dynamics in the BoB have been extensively studied by several researchers (Babu et al. 2003; Dey et al. 2017; Jana et al. 2018; Mandal et al. 2018; Shankar et al. 1996; Sharma et al. 2007; Shetye et al. 1993, 1996; Sil and Chakraborty 2011a, b; Vinayachandran et al. 1999). These studies have established that the ocean current along the western boundary is one of the dominant features in the BoB. It flows northward during spring (February to May), popularly known as the Western Boundary Current (WBC) and southward during autumn (September to November),

Responsible editor: Jin-Song von Storch

✉ Sourav Sil
souravsil@iitbbs.ac.in

[1] Ocean Analysis and Modeling Laboratory, School of Earth, Ocean and Climate Sciences, Indian Institute of Technology Bhubaneswar, Jatni, Odisha, India

[2] Present address: Department of Meteorology (MISU), Stockholm University, Stockholm, Sweden

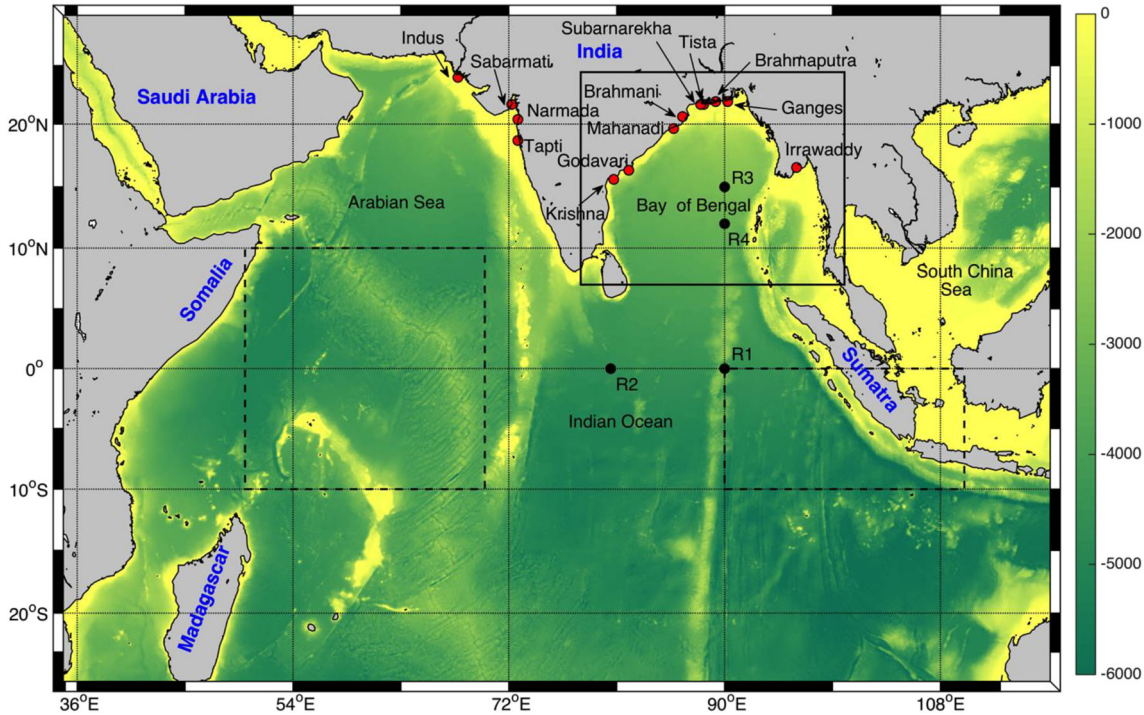

Fig. 1 The domain topography (m) of the Indian Ocean Model (IOM). Red points along the coastal boundary represent the locations of the river point sources. The black dot represents the RAMA buoy locations at R1 (0°N, 90°E), R2 (0°N, 80.5°E), R3 (15°N, 90°E), and R4 (12°N, 90°E). The solid rectangular box represents the boundary of the Bay of Bengal Model (BoBM) and dashed boxes are the western and eastern domains to calculate the Dipole Mode Index (DMI)

recognized as the East India Coastal Current (EICC). Other time of the year, the BoB circulation is well characterized by the cyclonic and anticyclonic eddies (Chen et al. 2012, 2018; Cheng et al. 2018).

In addition to the local winds and thermal forcing, circulation in the basin is influenced by remote forcing from the equator in terms of coastally trapped Kelvin waves (KWs) and the westward propagating Rossby waves (RWs) (Potemra et al. 1991; Shetye et al. 1996; Yu et al. 1991). The coastally trapped KWs in the BoB are the northern part of the bifurcated (from Sumatra coast) equatorial KWs. The RWs in the BoB are generated due to the reflection of coastal KWs from the eastern coast of the BoB. The coastal KWs have two alternating pair of upwelling (January–April and August–September) and downwelling (May–August and October–December) KWs that remotely affects the circulations in the BoB (Rao et al. 2010; Nienhaus et al. 2012; Sreenivas et al. 2012). Thermocline in the BoB is significantly influenced by the RW propagation from the eastern boundary (Girishkumar et al. 2013; Chatterjee et al. 2017; Shee et al. 2019).

The equatorial KWs are highly influenced by interannual climate modes such as the Indian Ocean Dipole (IOD) and El Niño Southern Oscillation (ENSO) (Chakravorty et al. 2014; Chowdary and Gnanaseelan 2007; Rao and Behera 2005; Sayantani and Gnanaseelan 2015; Somayajulu et al. 2003; Yu et al. 2005). Generally, the IOD events start developing from June and peak in October (Saji et al. 1999; Webster et al. 1999; Vinayachandran et al. 2002, 2009), whereas the ENSO events peak in November–January (Gnanaseelan et al. 2008; Neelin et al. 1998; Sayantani and Gnanaseelan 2015; Somayajulu et al. 2003). Among the four phases of the coastal KWs, the second downwelling (upwelling) KW is absent (weak) during El Niño (La Niña) years, whereas the second upwelling KWs (uKWs) strengthen during El Niño (EN) years both in the equatorial IO and BoB (Sreenivas et al. 2012). During the negative IOD (NIOD) event, the second uKWs do not develop while the second downwelling KWs (dKWs) strengthen due to the downwelling favorable westerly winds (Aparna et al. 2012; Sreenivas et al. 2012) in the equatorial IO. These studies concluded that IOD and ENSO primarily influence the sea level in the BoB through the coastal KWs. The sea surface height anomalies (SSHA) are the proxy for thermocline (Yu 2003; Sil and Chakraborty 2012). The variations of satellite-derived SSHA could be used to estimate the thermocline in the BoB.

The effects of the coastal KWs during IOD events on the upper ocean circulation features in the BoB have been also reported in the recent studies. During the NIOD, the equatorward EICC intensifies (Sherin et al. 2018), which is due to the stronger second dKWs (Dandapat et al. 2018). This leads to more freshwater transport than PIOD composite events (Fournier et al. 2017; Dandapat et al. 2018). Role of remote and local forcing on EICC dynamics during ENSO events are studied by Mukherjee and Kalita (2019). The coastal

upwelling and strong haline stratification lead to a thinner barrier layer thickness (BLT) over the eastern BoB during the PIOD events, whereas the coastal downwelling in the NIOD events leads to a deeper isotherm and thicker BLT (Kumari et al. 2017). The sea surface temperature (SST) and chlorophyll-a (Chl-a) concentration show negative (positive) anomalies during positive (negative) phases of IOD and ENSO events in the BoB (Devi and Sarangi 2017; Currie et al. 2013). The numbers of cyclones are more during La Niña (LN) events due to the increased ocean heat content in the BoB (Girishkumar and Ravichandran 2012). Note that the earlier studies have been carried out to identify the role of equatorial forcing on SSHA, SST, BLT, and coastal current variations in the BoB. But studies featuring their impacts on the thermocline and subsurface temperature variability in the BoB are very limited.

In this study, we have carried out two numerical experiments using Regional Ocean Modeling System (ROMS) to investigate the role interannual equatorial forcing on the (a) characteristics of interannual variations of SSHA in the BoB and (b) subsurface temperature variability in the BoB during both the phases of IOD and ENSO events. Available observations and reanalysis datasets are utilized to support the results. The paper is organized in the following manner. A brief description of the ocean model configurations and various observational datasets used in this study are described in Sect. 2. Section 3 comprises the validation of the model results. The variations of SSHA and subsurface temperature during different phases of IOD and ENSO and their influence on the frequency of cyclones and chlorophyll are discussed in Sect. 4. Finally, conclusions are reported in Sect. 5.

2 Model, data, and methodology

The ROMS is a hydrostatic, three-dimensional, sigma coordinate ocean model, which solves the primitive equations based on the vertical momentum balance and Boussinesq approximation in an Earth-centered rotating environment (Haidvogel et al. 2000; Penven et al. 2006; Shchepetkin and McWilliams 2003). The model configurations and experiments are described in Sect. 2.1. A brief description of the observational datasets is given in Sect. 2.2. The statistical quantities (Skill Score, Student's *t* test) used in this study are explained in Sect. 2.3.

2.1 Model configuration

Our goal is to understand the effect of equatorial forcing on the interannual variability of SSHA and thermocline in the BoB. Therefore, we have conducted two model experiments. In the first experiment, the model domain was taken 26°S–29°N, 34°E–118°E over the IO, so that the interannual equatorial effects can be considered. In the IO model (IOM), the horizontal grid spacing was 1/4° (eddy-permitting) in both the zonal and meridional directions with 42 sigma co-ordinate vertical levels (14 levels in upper 100 m at the maximum depth). The bathymetry fields were extracted from the Earth Topography 2-min (Etopo2, Smith and Sandwell 1997) datasets. For a better simulation of the surface and subsurface oceanic parameters, an enhanced resolution was assigned near the surface by defining the bottom stretching parameter (θ_b) = 0.58 and surface stretching parameter (θ_s) = 7.0 (Song and Haidvogel 1994; Shchepetkin and McWilliams 2005; Haidvogel et al. 2008). The minimum depth of the model was taken at 5 m.

The model domain had open ocean boundaries at the eastern and southern sides. The initial and interannual boundary conditions for temperature and salinity were taken from the global Simple Ocean Data Assimilation (SODA) (Carton and Giese 2008), which were extensively used previously for the IOD and ENSO studies (Li et al. 2017; Sayantani and Gnanaseelan 2015). Two different versions of the SODA data were used: version 2.2.4 during 1991–2010 and version 3.3.1 during rest of the period (2011–2015). The interannual open boundary conditions from a global model allowed us to include large-scale informations into the regional model. The interannual atmospheric forcing fields of wind stress, air temperature, and net heat flux were taken from the TropFlux (1° resolution) datasets (source: http://www.incois.gov.in/tropflux/index.jsp) for the period 1988–2015 (Kumar et al. 2012). The TropFlux data is suggested to be a suitable forcing for ROMS simulation in the BoB region (Dey et al. 2017). Interannual river runoff datasets (Dai 2016) from 13 rivers were included in the model simulation (see Fig. 1 for the locations of river points input along the coast), using the methodology described in Jana et al. (2015). Nine major rivers (the Ganges, Brahmaputra, Irrawaddy, Mahanadi, Godavari, Krishna, Teesta, Subarnarekha, and Brahmani) in the BoB and 4 rivers (Indus, Sabarmati, Narmada, and Tapti) in the Arabian Sea (AS) were considered in this study (source: http://www.cgd.ucar.edu/cas/catalog/surface/dai-runoff/). The interannual river data were used for the Brahmaputra and Indus rivers during 1988–2000, for the Ganges during 1988–1996 and for the Tista during 1988–1991. Climatological river data were used for these rivers for the remaining years. For all other rivers, climatological river data were used during the entire period of study. The K-profile parameterization (KPP) scheme was used for the vertical mixing (Large et al. 1994). The model was integrated for the time period 1988–2015. The volume-averaged kinetic energy of the model simulation revealed that the model takes 3 years to reach its dynamical equilibrium (figure not shown). Therefore, we analyzed the model results for the time period of 1991–2015 (25 years).

In the second experiment, we restricted our area of interest to the BoB (7°N–24°N, 80°E–100°E) only. In this BoB model (BoBM) experiment, the southern boundary conditions were

relaxed to monthly climatology of temperature and salinity, i.e., the same climatological boundary condition is applied every year. However, the interannual surface forcing fields from TropFlux are applied for the period 1988–2015. As the southern boundary is fixed at 7°N and interannual variability is absent at the boundary, the BoBM configuration precludes the effects of the interannual variations of equatorial remote forcing.

2.2 Observational datasets

The performance of the model at the equator was assessed using zonal currents from the Research Moored Array for African-Asian-Australian Monsoon Analysis (RAMA) observations at R1 location (0°N, 90°E) during 2001–2015 and at R2 location (0°N, 80.5°E) during 2005–2015 (source: https://www.pmel.noaa.gov/tao/drupal/disdel/). Temperature observations during 2008–2015 from two other RAMA buoys in the BoB at locations R3 (15°N, 90°E) and R4 (12°N, 90°E) were also used for validation of temperature in the BoB. The current observations at these locations were not continuously available; therefore, current could be not compared. The locations of all RAMA buoys are shown in Fig. 1. Advanced Very High-Resolution Radiometer (AVHRR) blended SST (source: http://www.ncdc.noaa.gov) datasets (horizontal resolution of 25 km) for the duration 1991–2015 (Reynolds et al. 2007) were used for validation of SST in the BoB. The Ocean Surface Current Analysis Real-time (OSCAR), which is a level 4 dataset with a horizontal and temporal resolution of 1/3° and 5 days respectively, were used for seasonal comparisons of the surface currents during 1993–2015 (Bonjean and Lagerloef 2002). The model simulated SSHA fields were compared with the satellite-derived Archiving Validation and Interpretation of Satellite Oceanographic (AVISO) monthly mean fields during 1993–2015 (source: http://marine.copernicus.eu/). Since the reference level for calculating SSH for ROMS was different from the reference level of AVISO SSHA (Strub and Corinne 2015), we have used the methodology described by Jana et al. (2018) for the comparisons of the SSHA fields. The simulated temperature in the BoB was compared with the Argo profiles during 2005–2015 (Argo 2019) after quality control (Wong et al. 2009; Dey et al. 2017; Sil and Chakraborty 2012). We have also used Argo gridded datasets (source: http://apdrc.soest.hawaii.edu/) during 2005–2015. The data for tropical cyclonic disturbances over the BoB was taken from the Regional Specialized Meteorological Centre (RSMC), Indian Meteorological Department (IMD), India (source: www.imd.gov.in/section/nhac/dynamic/cyclone.htm). In this study, we have considered the cases of depression (wind speed 17–27 kt) and above. The monthly Chl-a data for the duration 2003 to 2015 was taken from Moderate Resolution Imaging Spectroradiometer (MODIS) Aqua satellite (source: https://oceancolor.gsfc.nasa.gov/data/aqua/). Also, we have used the temperature data from European Centre for Medium-Range Weather Forecasts (ECMWF) Ocean Reanalysis System 4 (ORAS4) datasets (Balmaseda et al. 2013) (source: http://www.ecmwf.int/products/forecasts/d/charts/oras4/reanalysis/) to compare with the model subsurface temperature during 1991–2015.

2.3 Methodology

The composite years of positive and negative phases of IOD (PIOD and NIOD) and ENSO (EN and LN) were prepared based on the National Oceanic and Atmospheric Administration (NOAA) and Jongaramrungruang et al. (2017) (Table 1).

Nino 3.4 index was taken from NOAA. As we were interested in analyzing the IOD and ENSO events, which were dominant during September to May, we presented our results for three seasons; September to November (SON), December to February (DJF), and March to May (MAM) (Sayantani and Gnanaseelan 2015). The Dipole Mode Index (DMI) was calculated considering surface temperature anomalies in western (10°S–10°N, 50°E–70°E) and south-eastern (10°S–0°N, 90°E–110°E) boxes Indian Ocean (Saji et al. 1999). The boxes were indicated with dotted lines in Fig. 1. The thermocline variability over the BoB was studied in terms of D23 (the 23 °C isotherm depth) as suggested by Girishkumar et al. (2011), Girishkumar et al. (2013), and Jana et al. (2018).

Skill score was calculated from the correlation coefficient and standard deviations (Dey et al. 2017; Taylor 2001) by the following formula,

$$S = {}^{4(1+R)}\!/_{\left(\sigma+{}^{1}/_{\sigma}\right)^{2}(1+R_0)}$$

where R is the correlation coefficient and σ is the ratio of standard deviations. We use $R_0 = 0.99$, the maximum correlation attainable. All comparisons with the observations were carried out on the horizontal or vertical grids of the data having coarser resolutions. The indices were calculated by subtracting the mean value and taking normalization with

Table 1 Years of positive IOD (PIOD), negative IOD (NIOD), El-Niño (EN), and La-Niña (LN) during the study period

PIOD	NIOD	EN	LN	Normal year
1994	1992	1991	1995	1993
1997	1996	1994	1998	2001
2006	1998	1997	1999	2003
2012	2005	2002	2000	2004
2015	2010	2006	2007	2011
		2009	2008	2013
		2015		2014

respect to their standard deviations. The statistical significance was performed using Student's *t* test and all the correlation coefficients were 99.95% significant. To find out the dominant interannual modes of different parameter, empirical orthogonal function (EOF) analysis was performed on observed and simulated fields. All EOF analyses were done after removing the linear trend and seasonal cycle for the time series of each grid points. All anomalies calculated for different positive and negative phases of IOD and ENSO are with respect to the normal years.

3 Validation of ROMS

We first assess the IOM model at the equator to evaluate the capability of the model on the simulation of the equatorial processes (Sect. 3.1). Then, we assess the performance of the IOM model in the BoB domain (Sect. 3.2). We have not included the results for the BoBM in this section.

3.1 Model validation over equatorial IO

The ROMS simulated currents were compared with equatorial zonal currents from RAMA observations at R1 location (0°N, 90°E) during 2001–2015 and at R2 location (0°N, 80.5°E) during 2005–2015 (Fig. 2). The annual cycle was clearly observed with westward propagation of surface currents during February–March and June–September. The simulated and observed ocean currents displayed a pronounced oscillation in the upper 100 m, indicating the effect of eastward flowing semi-annual Wyrtki jet (Wyrtki 1973; Iskandar et al. 2009; Prerna et al. 2019) during spring (April–May) and fall (October–November). The smaller time scale variations in the upper ocean zonal currents are mainly due to the semi-annual wind forcing variability accompanied by the intraseasonal oscillation in the atmosphere (Senan et al. 2003; Masumoto et al. 2005; Nyadjro and McPhaden 2014). During NIOD (2005), the fall time Wyrtki jet was observed to be stronger than the normal years (2003 and 2004) from both RAMA observations and model simulations, which was clearly seen at R2 location and the results were well agreed with the studies by Sachidanandan et al. (2017) and Vinayachandran et al. (2002). Also, the speed of the fall Wyrtki jet decreased during PIOD (2006) event, which matched well with the findings of Gnanaseelan et al. (2012). The vertical structure of the jet showed a large interannual variability with the current speeds reached ~ 0.5 to 0.8 m/s at R1 location and ~ 0.5 to 1.5 m/s at R2 location during the peak phase of the jet.

The subsurface zonal currents at ~ 100 m showed substantial variations with a more extended time period. The equatorial undercurrent (EUC) (McCreary 1981; McCreary 1985; Schott and McCreary 2001; Chen et al. 2015, 2016) between 80 and 160 m was found to be stronger during January–May in both ROMS simulations (Fig. 2a) and RAMA observations (Fig. 2b). Eastward propagating EUC was dominating mostly during February–April and July–October, and subsurface currents were towards the west during the rest of the period. At the upper ocean levels, the model simulated zonal currents had slightly higher magnitude. Interestingly, for total currents, the depth-wise correlation was greater than 0.7, the skill was greater than 0.8 and root mean square errors (RMSEs) were very less (~ 0.0–0.1 m/s) throughout the depths at both locations (Fig. 2e, f, solid line). When the seasonality has been removed, the interannual part of the currents showed a correlation more than 0.4 throughout the depth at both locations

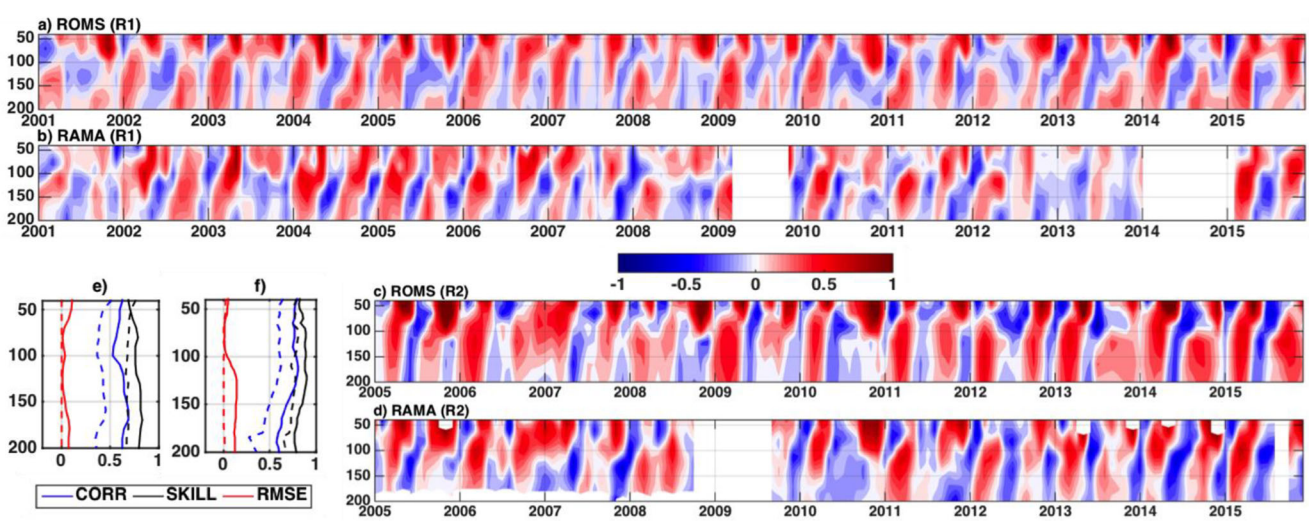

Fig. 2 Comparisons of equatorial zonal currents (m/s) from ROMS simulation and RAMA buoy observations at 90°E (**a**, **b**) and 80.5°E (**c**, **d**). Westward (eastward) currents are represented by blue (red) shades. Depth wise correlation (blue line), skill (black line), and RMSE (red line) of total currents (solid line) and interannual currents (after removing seasonal signals) (dashed line) between RAMA and ROMS simulated zonal currents at **e** 90°E and **f** 80.5°E

(Fig. 2e, f, dashed line). The correlation values are statistically significant at 99% confidence level as determined by *t* value. These comparisons suggest that the configured ROMS model for the IO was capable enough to simulate the observed interannual ocean current variations at the equator.

3.2 Model validation over the BoB

The IOM simulated seasonally averaged SST, and surface currents were compared with the AVHRR blended SST and OSCAR surface currents (Fig. 3a–f). The magnitude and direction of the model simulated ocean surface currents agreed with the observational datasets. IOM well simulated the winter monsoon current over the southern BoB during DJF. The northward propagating WBC (Gangopadhyay et al. 2013) on the western boundary of the basin during MAM was well captured in the model (Fig. 3c, f). A cyclonic eddy was simulated in the ROMS at around 15°N on the western BoB during SON. This was also observed from OSCAR currents, but with weaker amplitude.

Moreover, the EICC was reasonably well simulated along the western boundary of the BoB (Fig. 3a, d). The cyclonic eddy on the southwestern BoB was nicely simulated in the model, which reduced the temperature in that region due to upwelling (Fig. 3a, d). This eddy persisted till DJF as seen from both the model and observations (Fig. 3b, e). The simulated westward North equatorial current (NEC) on the southern BoB was also well captured in the model during DJF. Later in MAM, the NEC bifurcated near Sri Lanka resulted in the formation of WBC (Fig. 3c, f).

The model showed a qualitative agreement on simulating the seasonal and spatial variations of SST over the BoB. A cold bias (~ 0.4 °C) was observed over the northern BoB during SON (Fig. 3a) and over the southwestern BoB during DJF (Fig. 3b). To quantify the biases in the northern and southern BoB, average SST over the northern (north of 15°N) and southern (south of 15°N) BoB were analyzed during 1991–2015 (figure not shown). The RMSEs in the northern and southern BoB were 0.41 °C and 0.04 °C respectively, although correlation and skill in both the domain were greater than 0.89. The biases in the northern BoB were possibly due to net heat flux in the TropFlux datasets (Dey et al. 2017). However, the SST was well simulated over the central and south-eastern BoB.

For the interannual variations, the ROMS simulated domain averaged (75–100°E and 4–24°N) temperature (at 5 m)

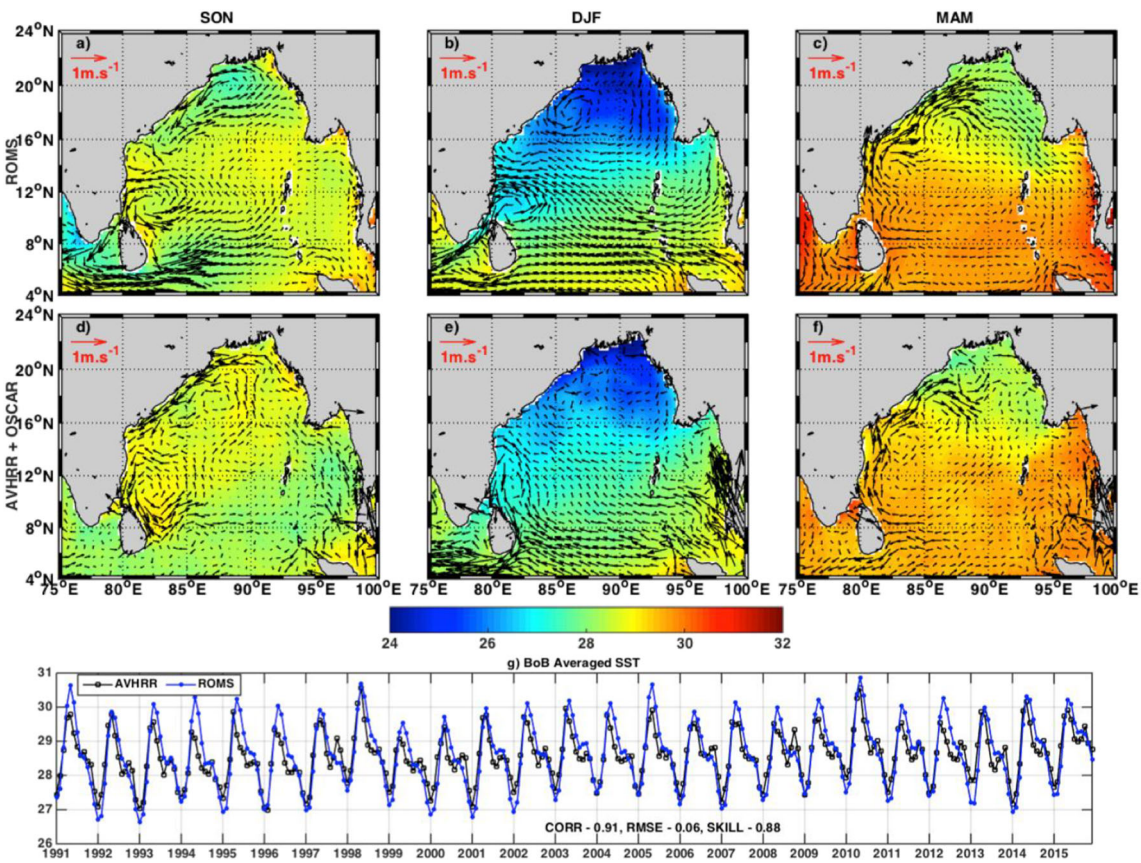

Fig. 3 Comparison of seasonally averaged SST (°C, shaded) and surface currents (m/s, vectors) during 1991–2015 from ROMS (1st row) with AVHRR blended SST and OSCAR currents (2nd row) in SON (1st column), DJF (2nd column), and MAM (3rd column). **g** The BoB averaged SST (°C) from ROMS (blue line) and AVHRR blended SST during 1991–2015 (black line). Only results from IOM are shown here

was compared with the AVHRR blended SST (during 1991–2015) (Fig. 3g). The comparison showed a good correlation (0.91) with less RMSE (0.06 °C) and higher skill score (0.88). Note that, during the positive phases of IOD and ENSO (Table 1), the SST was colder than that of normal years during SON and DJF, and during the negative phases, the SST was warmer in the BoB (Fig. 3g), which agreed with the results of Devi and Sarangi (2017). Model skills indicated a higher value (0.88) on simulated SST pattern over the BoB.

Additionally, we also compared the subsurface temperature with associated statistics at two RAMA buoy locations R3 (15°N, 90°E) and R4 (12°N, 90°E) in the BoB. Vertical distributions of temperature matched very well up to 100 m with less RMSEs (< 0.3 °C) and moderate skill (> 0.6) (Fig. 4). Below 100 m, the RMSEs were higher (1 °C for R3 and 1.4 °C for R4 locations) with decent skill score of ~ 0.5 up to ~200 m depths. These comparisons confirmed the ROMS ability on efficient reproduction of the seasonal variations of ocean surface temperature and currents.

4 Results and discussion

In this section, the interannual variability of SSHA and thermocline in the BoB domain from two model experiments are discussed. The characteristics of the coastal KWs are analyzed from the SSHA variability in Sect. 4.1. The subsurface temperature variation is also explained during positive and negative phases of IOD and ENSO events as simulated in the model experiments (Sect. 4.2). Their validations with observations are discussed in Sect. 4.3, and their impact on cyclone and productivity are discussed in Sect. 4.4.

4.1 Interannual variability of SSHA over BoB from models and observation

In this section, we have presented the interannual variability of the BoB SSHA and found its relationship with the equatorial forcing. The SSHA is a significant indicator of IOD and ENSO signatures over the BoB (Somayajulu et al. 2003; Aparna et al. 2012). It is important to note that both the models were capable to capture the observed seasonality when seasonal signals were not removed (Fig. 5a–c). Also, the EOF1 of simulated temperatures at 100 m (contours) from IOM matched well with the variability of sea level anomaly (Fig. 5c). The corresponding PC1 showed the seasonal cycle (Fig. 5d), which was consistent for the SSHA from models and observation.

To find out the dominant interannual modes of SSHA, EOF analysis was performed on the linear trend and seasonal signal removed SSHA from AVISO observation and from both models (Fig. 5e–g). The annual, semi-annual, and 4-month signals are filtered out on removing the seasonality, which is confirmed by the fast Fourier transformation (FFT) analysis (figure not shown). The spatial pattern of the first dominant mode of EOF analysis (EOF1) displayed an east-west variation of SSHA with the strong negative pattern along the pathway of coastal KWs and positive pattern over the southwestern BoB, from both AVISO and IOM (Fig. 5e, f). But this dipole structure was absent in the BoBM (Fig. 5g). In fact, it showed a very strong and extended pattern in the northern BoB, possibly due to the local winds and eddy dynamics in this region (Cheng et al. 2018). Apart from this, the variance of EOF1 from AVISO and IOM were 33.1 and 27.7%, respectively, whereas the variance of EOF1 from BoBM was very less (12.9%).

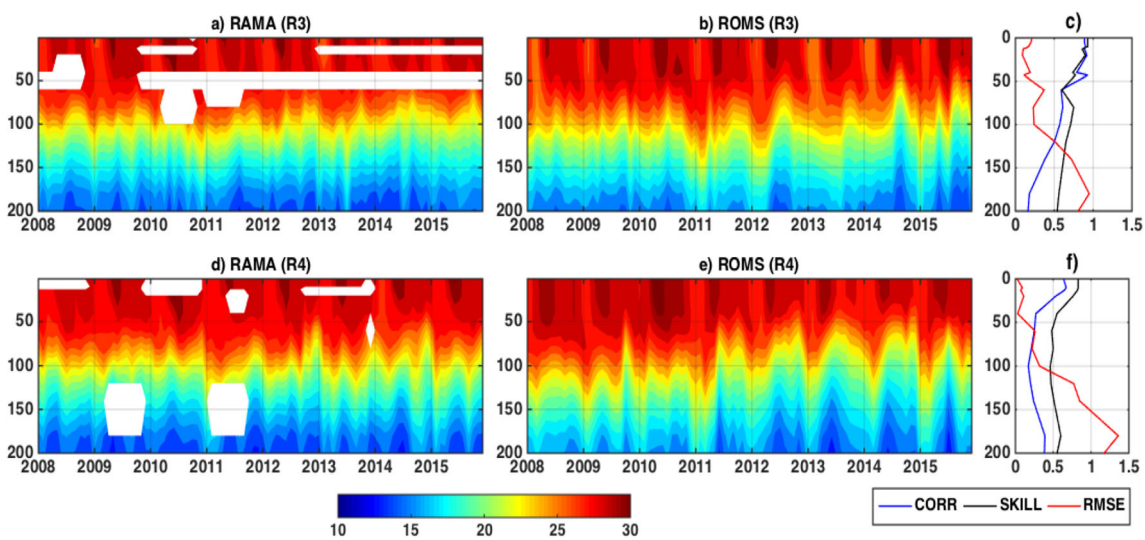

Fig. 4 Comparison of time-depth temperature variation from RAMA and ROMS at two locations at R3 (15°N, 90°E) and at R4 (12°N, 90°E) over the BoB with vertical profile of correlation (blue line), skill (black line) and RMSE (red line) between RAMA and ROMS at the respective locations are shown in the right panel

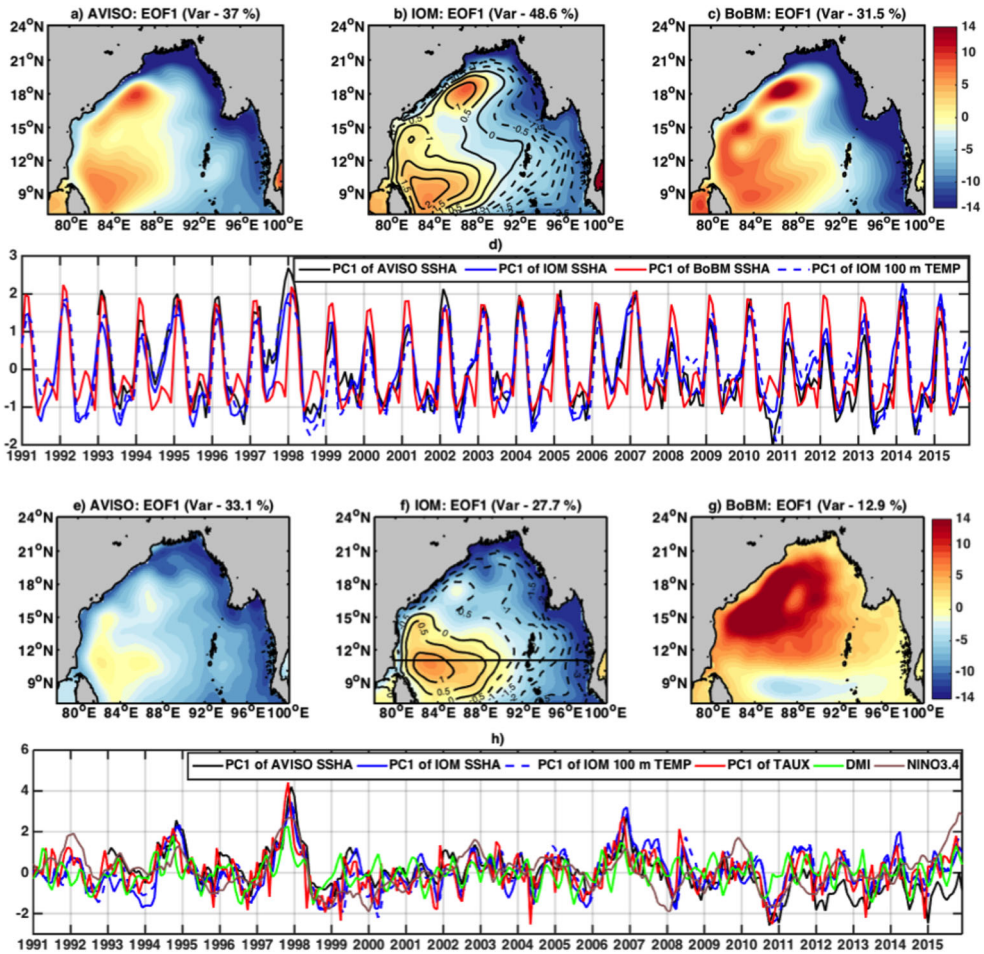

Fig. 5 EOF1 map of SSHA field without removing seasonal cycle from **a** AVISO, **b** IOM, and **c** BoBM. EOF1 of 100-m temperature from IOM are denoted by black contours in Fig. 5b. Solid and dotted lines represent the positive and negative contours, respectively. **d** Time series of first principal component (PC1) from without removing seasonality of AVISO SSHA (black line), IOM SSHA (blue line), and BoBM SSHA (red line). Third row (**e**–**g**) is same as first row (**a**–**c**) but after removing seasonal cycle. **h** Comparison of PC1 from AVISO SSHA (black line), IOM SSHA (blue line), 100 m temperature (blue dashed line) over the BoB and TAUX over the equator (1°S–1°N, 45–105°E) with DMI (green line) and Nino3.4 index (purple line) during 1991–2015. The black line along 11°N represents the averaged region (10°N–12°N) where the subsurface temperature and D23 are analyzed in Sect. 4.2

Since the equatorial zonal wind stress is the main dominating force to generate the equatorial KWs (Wyrtki 1973; Prerna et al. 2019), we had computed the first principal component (PC1) of equatorial zonal wind stress over the region 1°S–1°N, 45–105°E and compared with the PC1 of simulated SSHA, and DMI calculated from the IOM (Fig. 5f). The PC1 of BoBM simulated SSHA was not shown, as BoBM was unable to capture the interannual mode and showed only annual variation. The PC1 of SSHA from AVISO and IOM matched significantly well with a correlation coefficient of 0.68, which was one insight into the validation of the SSHA field from the model with AVISO observations. Also, a good correlation (0.68) between PC1 of equatorial zonal wind stress and SSHA from the IOM confirms the role of equatorial zonal winds in the SSHA variability over the BoB, through the equatorial and coastal KWs. The time series of DMI showed similar variations with PC1 of SSHA from IOM, lagged by 1 month with a lag correlation of 0.41 (Fig. 5h). The peak of PC1 from IOM as well as from AVISO SSHA was observed during October–December (OND), after the peak of DMI in September.

To study the effects of IOD and ENSO on SSHA variability over the BoB, we had analyzed the SSHA variations during the peak time of PC1 (October–December) in different composite events. The equatorial winds during September to May are shown in the Fig. 6 (1–5) during various events. Note that, the second dKWs associated with positive SSH were dominant over the BoB during OND (Rao et al. 2010). So, we had only presented the positive SSHA values of IOM (shaded) and AVISO (contours) in Fig. 6 (6–10) during OND of positive and negative phases of IOD and ENSO composite (Table 1). In the normal years, the second dKWs propagated along the eastern coastal rims of the BoB from October to December. The effects could be seen till 12°N along the western boundary (Fig. 6 (6)) due to the favorable westerlies at the equator (Fig. 6 (1)). During PIOD and EN composites, the second dKWs over the BoB were very weak (Fig. 6 (7 and 9)) as the equatorial westerlies during September–December are replaced by weak easterlies (Fig. 6 (2 and 4)).

On the other hand, during NIOD and LN composites the equatorial westerlies were stronger than the normal years (Fig. 6 (3 and 5)), which enhanced the second dKWs during OND to reach further south on the western boundary (Fig. 6 (8 and 10)). Note that the westward downwelling RWs associated with positive SSHA along 11°N are found relatively more extended till 84°E (Fig. 6 (7 and 9)) during PIOD and EN events from IOM to the local easterlies (figure not shown).

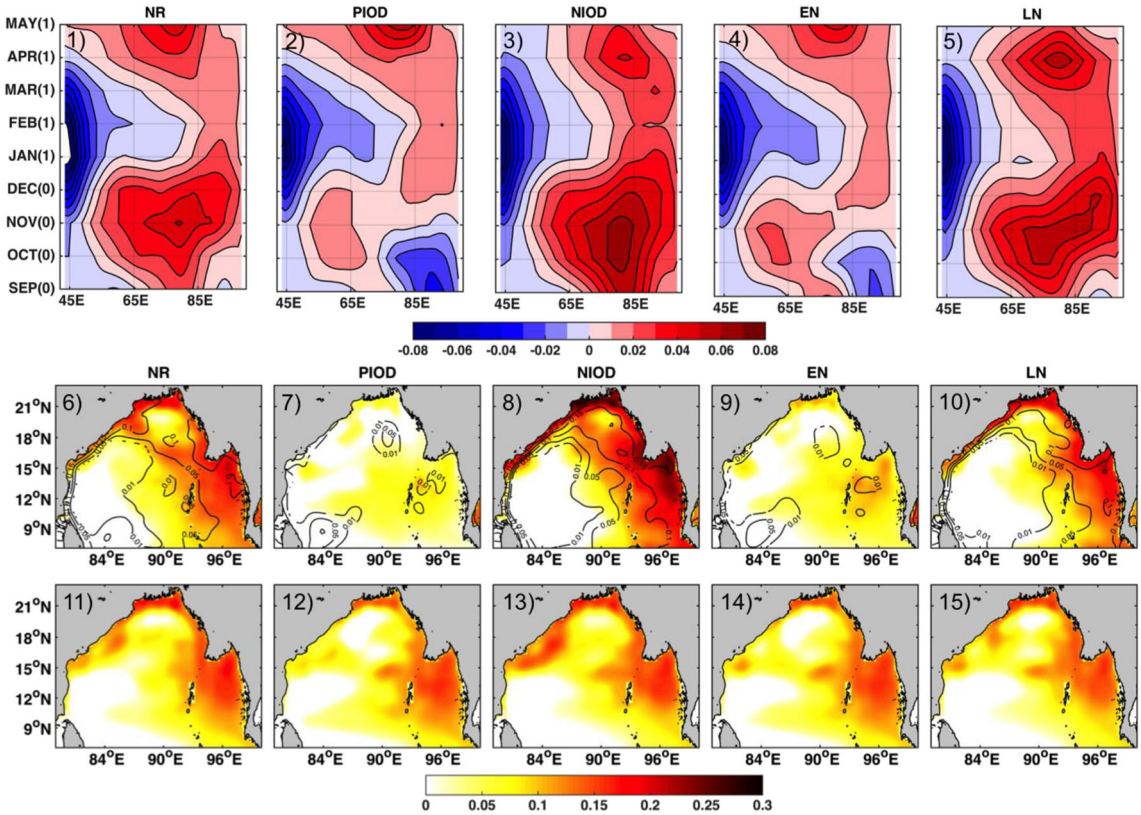

Fig. 6 Equatorial zonal wind stress during September (0) to May (1) in NR, PIOD, NIOD, EN, and LN composites (top row). Along Y-axis of the figure in the upper panel, months with (0) mean the year of IOD/ENSO event and (1) means months of the following calendar year. Comparison of SSHA from IOM (shaded) and AVISO (contours) (6 to 10) and from BoBM (11 to 15) during October–December in the phase of the 2nd dKWs

The impact of this variation on ocean thermal structure and thermocline is discussed in the following sections.

The variation of the 2nd dKWs in the BoBM, where the southern boundary condition was relaxed to climatology, was almost similar in all events (Fig. 6 (11–15)). However, the positive SSHA due to the coastal dKWs was found to move southward on the western boundary of the BoB during normal and NIOD composites (Fig. 6 (11 and 13)), whereas less in PIOD and EN composites (Fig. 6 (12 and 14)). The propagation of the RWs was found to be strong during positive phases of the events (Fig. 6 (12 and 14)). These experiments clearly indicate the impact of the equatorial forcing on enhancing (reducing) the propagation of 2nd dKWs during negative (positive) phases of IOD and ENSO events.

4.2 Role of local and remote forcing on subsurface temperature variability

Based on the EOF1 map, the vertical structures along the latitude of 11°N (averaged between 10°N to 12°N) were analyzed during SON, DJF, and MAM in IOD and ENSO composites from both the simulations. The wind stress curl along the same section from September to March during different events is shown in Fig. 7 (16–18). These figures showed an upwelling favorable wind stress curl (positive curl) during OND with comparatively higher magnitudes on the western side in the normal composites. During the negative phases, it was extended both in time (up to February) and longitude (up to 95°E). The following sections discussed the subsurface temperature variability for IOM in Sect. 4.2.1 and for BoBM in Sect. 4.2.2. Also, the propagation of Rossby waves associated with D23 and SSHA are analyzed in Sect. 4.2.3.

4.2.1 Subsurface temperature variability in IOM

In the normal years, a longitudinal asymmetry in the thermocline (D23) variability was observed (black line) with a deeper thermocline (~ 80 m) in the east and comparatively a shallower thermocline (~ 30 m) in the west during SON (Fig. 7 (1)). During DJF, a deeper thermocline from the east started moving westward (Fig. 7 (2)) and reached near 82°E in MAM (Fig. 7 (3)). During PIOD, the deepest thermocline (~ 70 m) was observed around 90°E (Fig. 7 (4)), which further propagated westward during DJF (Fig. 7 (5)) and reached the west coast of BoB during MAM (Fig. 7 (6)).

Conversely, in NIOD, the eastern BoB experienced a comparatively deeper thermocline (~ 100 m) very close to the coast in SON (Fig. 7 (7)) due to stronger second dKWs (Fig.

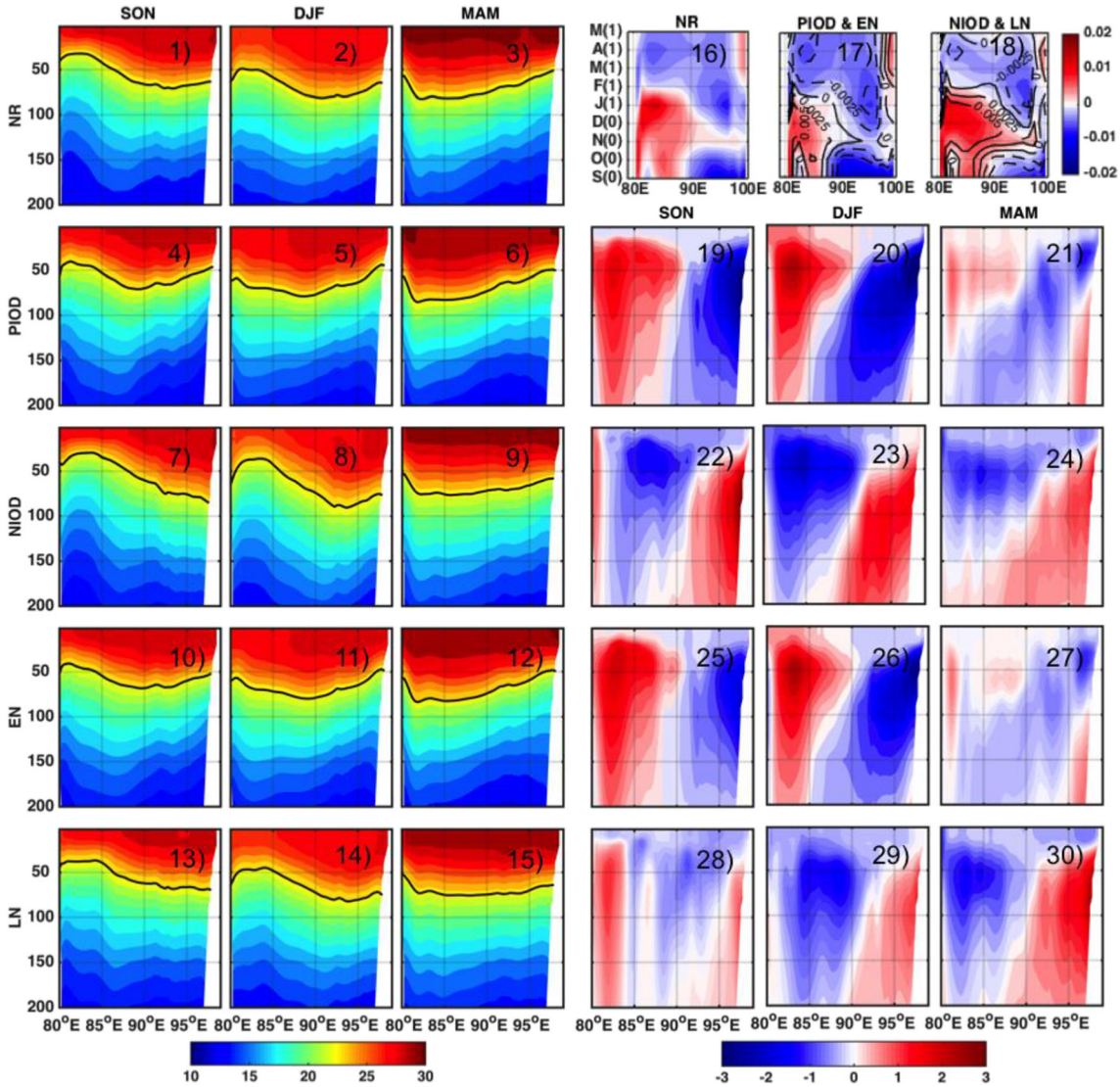

Fig. 7 Depth–longitude plots for temperature from IOM (first three columns, 1–15) during NR, PIOD, NIOD, EN and LN composites (top to bottom) and anomaly fields (last three column, 16–27) with respect to normal years along 11°N. The solid black line in temperature plot represents D23 (mean thermocline depth). Wind stress curl (N/m^3) along the same latitude during NR, PIOD (shaded) and EN (contours), NIOD (shaded) and LN (contours) are shown in 16–18, respectively

6 (8 and 10)) and stronger westerlies at the equator (Fig. 6 (3 and 5)). It was observed that the nature of thermocline variability during EN (Fig. 7 (10–12)) was similar to PIOD, and during LN, it was identical to NIOD (Fig. 7 (13–15)). The Fig. 7 (19–30) indicated the temperature anomalies with respect to the normal year along the same section during different events. During all the events, a dipole nature was observed in the subsurface temperature from 30 m to 150 m depth with 90°E at the center. This dipole nature developed in SON and diminished in MAM. During PIOD, the negative temperature anomalies were observed on the eastern side due to shallower thermocline as compared to the normal years (Fig. 7 (19 and 20)). This is due to the weaker second dKWs (Fig. 6 (7)) and weak westerlies (Fig. 6 (2)) at the equator. During the positive phases, a lower magnitude of the wind stress curl was observed than that during the normal years along the western BoB (Fig. 7 (17)), which led to weak upwelling. Whereas during the negative phases, the wind stress curl increased (Fig. 7 (18)) to make the upwelling stronger and negative temperature anomaly was noted on the western BoB.

During PIOD events, the negative subsurface temperature anomalies propagated westward (up to 85°E) in DJF (Fig. 7 (20)) and reached the western boundary in MAM (Fig. 7 (21)) below the warmer anomalies. During NIOD, the thermocline was deeper on the eastern coast (Fig. 7 (22 and 23)) due to the intense 2nd dKWs (Fig. 6 (8)) and favorable westerlies (Fig. 6 (3)). This made the temperature warmer on the east. The EICC on the western boundary intensified and made the cyclonic eddy on the southwestern BoB (Fig. 3a) stronger to enhance the upwelling and cold temperature anomaly on the west (Fig.

7 (22 and 23)). The negative anomalies were spread to the east at ~50 m during MAM (Fig. 7 (24)). The thermocline variation and temperature anomalies during EN (Fig. 7 (25–27)) and LN (Fig. 7 (28–30)) events were similar to variations during PIOD and NIOD events, respectively. So, the dipole nature of the subsurface temperature associated with thermocline depth was observed between eastern and western BoB.

The negative subsurface thermocline anomalies in the eastern bay during PIOD and EN are due to the westward propagating RWs radiated from the early initiated 2nd uKWs (Sreenivas et al. 2012) along the east coast of the BoB. During these events, the negative wind stress curl anomalies were observed along the western BoB (Fig. 7 (17)). So, the western bay is dominated by deeper thermocline with positive temperature anomalies. On the other hand, during the NIOD and LN years, the 2nd uKWs were not developed whereas, the 2nd dKWs were stronger than the normal years (Fig. 6 (8 and 10)). So, the positive subsurface temperature anomalies in the western bay are due to the leading edge of the radiated dRWs during NIOD and LN composites. Again, during the same composites, the positive wind stress curl anomalies (Fig. 7 (18)) and southward coastal currents intensified to strengthen the cyclonic eddy on the southwestern BoB. It helped to shallow the thermocline and cool down the subsurface temperature.

4.2.2 Subsurface temperature variability in BoBM

The thermocline variation was not prominent from the vertical sections of temperature in the BoBM (Fig. 8 (1–15)) during different events, as observed in the case of IOM. The westward propagation of higher temperature contours was observed during DJF and MAM in all events. In general, the D23 line is deepest on the eastern side during SON and it moved to the west side during MAM.

Due to weakening the positive wind stress curl on the western BoB (Fig. 7 (17)), the positive temperature anomalies were observed below 50 m depth in PIOD and EN composites on the western BoB extended to 90°E (Fig. 8 (16–18) and (22–24)), which was similar to the results from IOM (Fig. 7 (20 and 26)), but the values of the anomalies were less for BoBM. During these events, the negative anomalies on the eastern side were absent, due to the absence of 2nd dKWs

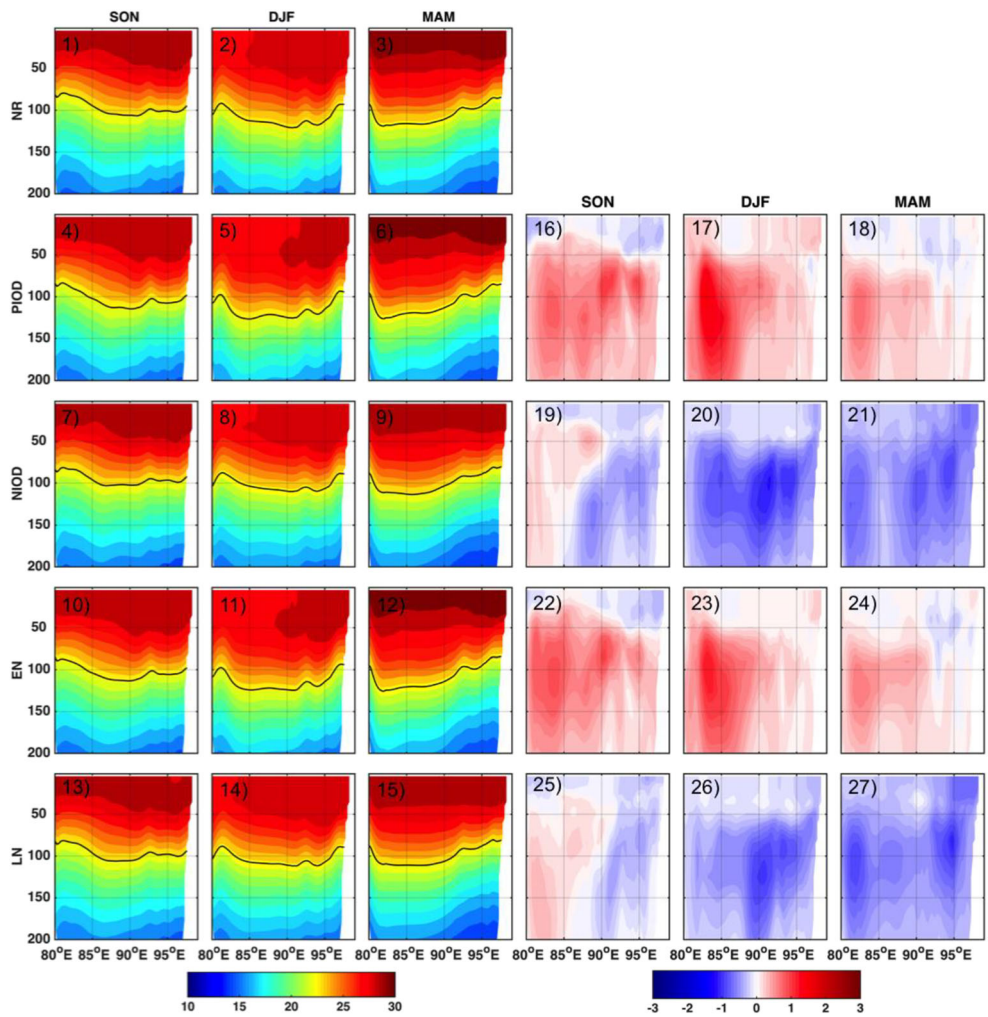

Fig. 8 Depth–longitude plots for temperature from BoBM (first three columns, 1–15) during NR, PIOD, NIOD, EN and LN composites (top to bottom) and anomaly fields (last three column, 19–21) with respect to normal years along the 11°N. The black solid line in temperature plot represents D23 (mean thermocline depth)

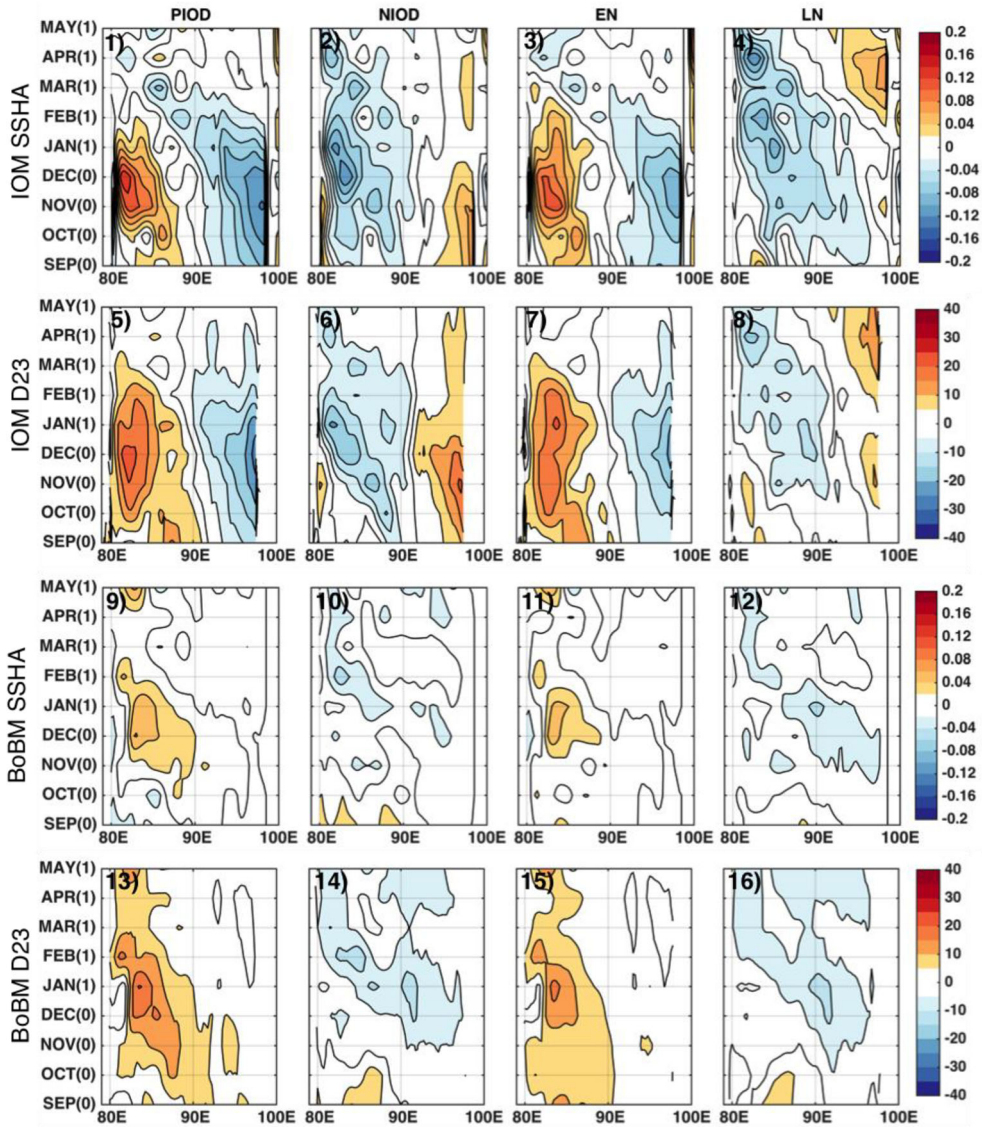

Fig. 9 Hovmöller (time-longitude) diagram of anomalous (normal year subtracted) SSHA (m) and D23 (m) from IOM (first two panels) and BoBM (last two panels) along 11°N during September (0) to May (1) during PIOD, NIOD, EN and LN composites

from the equator. These anomalies were confined on the western side of the section in case of IOM and magnitude of the anomaly was less for BoBM. In addition, the 2nd dKWs were not that strong as in IOM to deepen the thermocline, which made the water column cooler. Therefore, it determines the role of equatorial forcing in the BoB on modulating the thermocline on the eastern side of the basin and the local forcing on the western side of the basin during different events of IOD and ENSO. To understand the role of RWs, we discussed the westward movement of the SSHA and D23 along the same section during different events.

4.2.3 Rossby wave propagation associated with of SSHA and D23 during different events

The westward motion of the thermocline along the same latitude band is also analyzed, which is mainly due to the westward propagating of dRWs. Theoretical RWs speed along 11°N was 10 cm/s using the formula given by Prasanna Kumar and Unnikrishnan (1995), whereas average RW speed during 1991–2015 is observed ~ 8 cm/s from the slope of D23 in Hovmöller diagram for IOM (figure not shown). The comparisons of SSH and D23 anomalies along the same latitude from two simulations are depicted in Fig. 9. During PIOD and EN, the positive anomalies on the west of 90°E indicated stronger westward propagating dRWs and warming of the western BoB from the SSHA (Fig. 9 (1 and 3)) and D23A (Fig. 9 (5 and 7)) in the IOM. The negative anomalies in D23 were noted during NIOD and LN events (Fig. 9 (6 and 8)), which indicated enhanced upwelling and cooling of western BoB. Figure 9 also denotes a dipole nature of the D23 along the 11°N as observed in the EOF1 map of SSHA (Fig. 5f). The dipole structure was found to be developed from late September and persisted till March end. The peak intensity

of the dipole was observed during OND both from SSHA and D23A. During PIOD (Fig. 9 (5)) and EN (Fig. 9 (7)), the western side exhibited a deeper thermocline than the eastern side. While during NIOD, the opposite nature was observed in both the parameters. During LN, the variation is similar to NIOD. However, the signatures were weak in SON and DJF but more prominent in MAM (Fig. 9 (8)).

The variations of SSHA (Fig. 9 (9–12)) and D23 (Fig. 9 (13–16)) were very weak in the BoBM. During the positive phases, the westward movement of D23A was noted (Fig. 9 (13 and 15)) from 90°E, while during the negative phases, the westward motion of the negative D23A was observed from extreme east (Fig. 9 (14 and 16)). Therefore, during negative events, the negative temperature anomalies were observed throughout the region, whereas, during the positive events, a positive anomaly was observed only along the western side of the BoB.

4.3 Subsurface temperature dipole from observations and reanalysis products

To substantiate the subsurface temperature variations in the real ocean, we compared the IOM simulated results with the Argo profiles. Two regions were identified: 8–13°N, 81–86°E in the western region (named as Box – W) and 8–13°N, 91–96°E in the eastern region (named as Box–E) as per EOF1 map (Fig. 10a). But the numbers of Argo profiles were comparative very less in Box–E (Fig. 10b). Therefore, another region 16–21°N, 87–92°E in the Northern BoB (named as Box–N), showing similar variations (negative pattern) in the EOF1 map and having ample number of Argos, was selected for analysis instead of the Box-E. The temperature anomaly of the Box-E (contour) and the Box-N (shaded) from the IOM simulation showed the similar variation (Fig. 10e). After quality control, total numbers of Argos during September (0)–February (1) in Box–E, Box–N, and Box–W from 2005 to 2015 are shown in Fig. 10c.

The time-depth variation of temperature from Argo and IOM in the boxes were analyzed from 2005 to 2015. In PIOD years (2006, 2012, and 2015) and EN years (2006, 2009, and 2015), positive temperature anomalies were observed in Box-W, whereas, negative in Box-N from both the Argo observations (Fig. 10d, f) and IOM (Fig. 10e, g). Conversely, the positive (negative) temperature anomalies were observed in Box-N (Box-W) during the NIOD years (2005 and 2010), and LN year (2007 and 2008). Note that, during a concurrent year (2015) of PIOD and EN, strong positive and negative temperature anomalies were observed in Box-W and Box-N, respectively. The ROMS simulated results matched well with the temperature variations as obtained from Argos. But the range of the temperature variations was found to be more in Argo. The core of the warming and cooling were

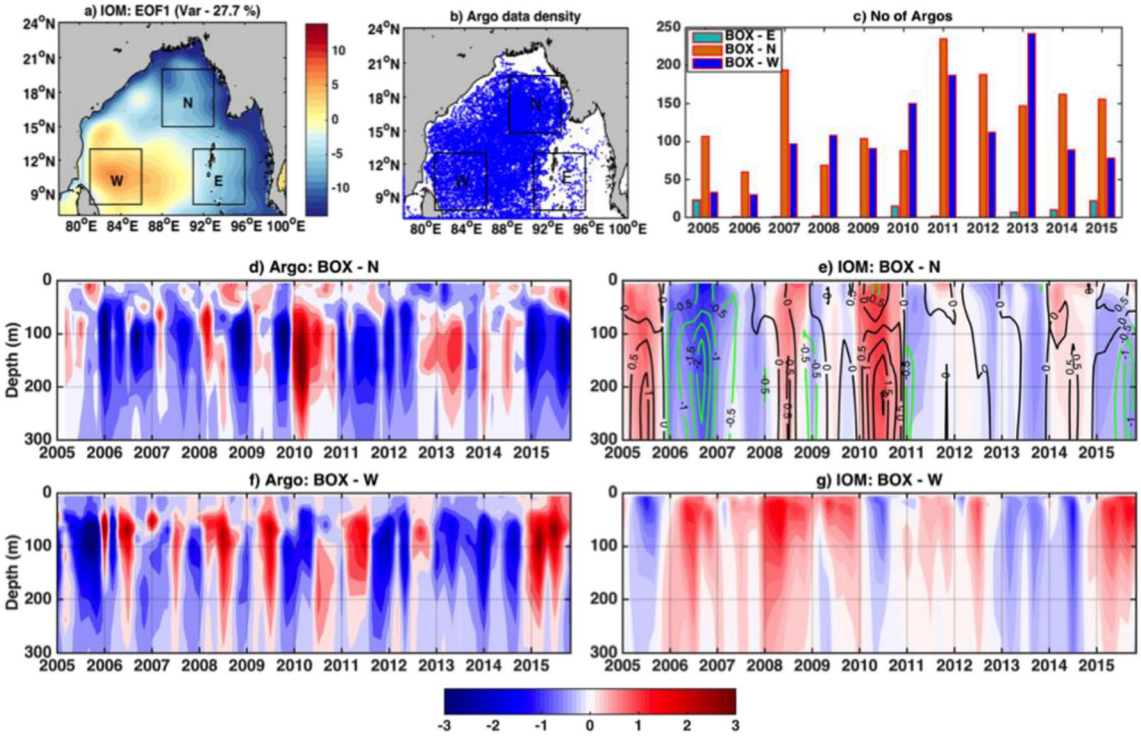

Fig. 10 **a** EOF1 map of seasonality removed SSHA from IOM. **b** Argo data density during 2005–2015 in the BoB. **c** Total number of Argo floats during September (0) to February (1) in Box-E, Box-N, and Box–W. **d–g** Temperature variations during the same time in Box-N and Box-W from IOM and Argo observations as denoted at the title of each panel. The black (green) contours in the panel **e** denote the positive (negative) temperature anomalies for BOX-E from IOM

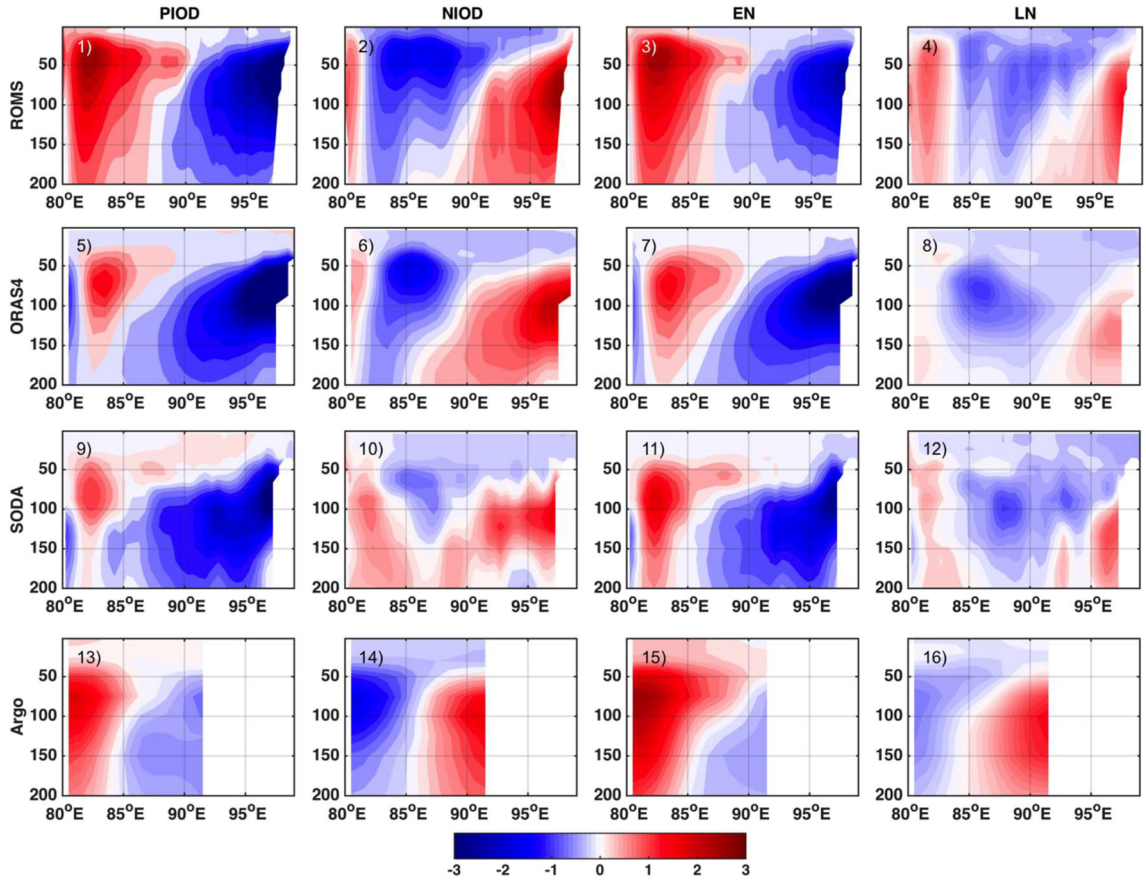

Fig. 11 Depth–longitude plots for temperature anomalies (normal year subtracted) from IOM (1–4), ORAS4 (5–8), SODA (9–12), and Argo (13–16) datasets during October–December (OND) in PIOD, NIOD, EN, and LN composites

noted between 30 to 150 m from both the Argo observations and model. These comparisons of the model with Argo observations confirm the dipole nature of the subsurface temperature over the BoB during the interannual climatic events. The comparisons also showed the peak dipole nature during OND.

For further validation of the results, the variation of temperature anomalies along 11°N from ROMS (Fig. 11 (1–4)) was also validated against ORAS4 (Fig. 11 (5–8)), SODA (Fig. 11 (9–12)) and available Argo gridded datasets (Fig. 11 (13–16)) during different events. These observed datasets showed similar temperature variability as the IOM, but positive temperature anomalies during PIOD and EN composites in the western BoB was bounded up to 83°E (Fig. 11 (1 and 3)). Among them, ROMS, ORAS4, and Argo gridded product showed a distinct dipole in the thermocline.

4.4 Quantification of dipole in BoB and its applications

The previous sections indicated the peak impact of the IOD and ENSO events, with the core of the dipole at ~ 100 m during OND. In addition, the EOF1 map of 100 m temperature simulated from IOM showed similar results (Fig. 5f contours). Therefore, we investigated the spatial pattern of the 100 m temperature anomalies (shaded) and D23 anomalies (contours) to visualize the spatial extent of the subsurface dipole (Fig. 12a–d) during OND. This feature on the east also extended up to the Northern BoB, which can also be observed in the subsurface temperature anomalies from the Argo observations. The temperature difference between the north-eastern and western BoB varies between − 3 and 3°*C*. The positive (negative) temperature anomalies over the western BoB extended up to 16°N over the western BoB during PIOD (NIOD) and EN (LN) composites. Moreover, the longitudinal extensions were not the same during the positive and negative phases. During the positive phases (PIOD and EN composites), the positive temperature anomalies extended up to 90°E but, during the negative phases (NIOD and LN composites) the negative temperature anomalies were spread up to 93°E. Except for the western part, the remaining portion of the BoB experienced negative (positive) temperature anomalies during PIOD (NIOD) and EN (LN) composites.

The variability of the thermocline depth (D23) also supported the dipole nature of the subsurface temperature in the BoB. During PIOD (NIOD) events, the D23 anomalies were ~ 10 m deeper (shallower) in the south-western BoB. It was

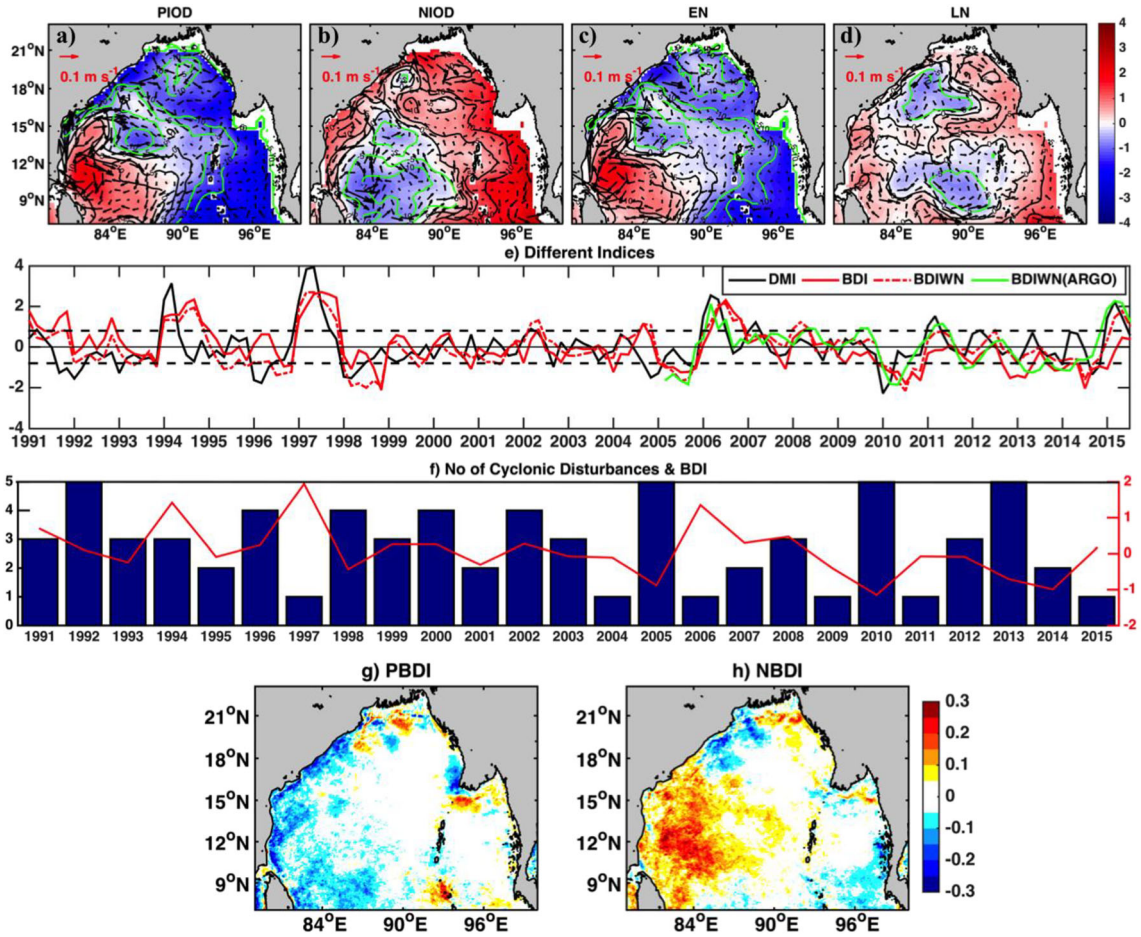

Fig. 12 Anomalies fields of IOM simulated 100-m temperature (°C, shaded), thermocline depth (m, contours) with currents (vectors) at 100 m depth during differ IOD-ENSO events (**a**–**d**). Green (black) contours represent the negative (positive) thermocline depth anomalies. **e** Time series of different dipole indices such as DMI (black line), BDI with respect to Box–W and Box–E (red solid line) from IOM, BDIWN with respect to Box–W and Box–N (red dotted dashed line) during September (0) to February (1) from IOM and from Argo observation (green line). Black dashed horizontal lines denote the ±1 standard deviation of BDI. **f** Number of cyclonic disturbances (depressions and above, in bar) and BDI (red line, y-axis in right side) plot during post-monsoon seasons (October–November). Chlorophyll-a concentration (mg/m^3) anomalies from MODIS Aqua during the post-monsoon time during **g** positive BDI (PBDI) and **h** negative BDI (NBDI) composites

observed that the cyclonic eddy on the north of Sri Lanka during DJF (Fig. 3b) weakens in case of the PIOD and EN events as the vector anomalies show opposite directions (Fig. 12a, c). However, the same eddy intensified during the NIOD and LN events to make the D23 shallower with negative temperature anomalies. Similarly, the opposite pattern was observed in the northern BoB. However, during the EN and LN years, the variation of D23 is ~ 5 m, which was lesser as compared to the other two events. It was also noted that the strengthening of NEC during PIOD and EN events led to the formation of WBC earlier than the other events (Iskandar et al. 2009; Rao et al. 2010), which is due to the strengthening of RWs. This also helps to make the D23 deeper and warmer 100 m temperature.

To quantify the intensity of this dipole, we had defined a new dipole index namely the BoB dipole index (BDI) as the normalized difference in 100 m (which means averaged depth of the core of the dipole and mean D23) temperature anomalies between the Box–W and Box–E along the same latitude belt. However, we had also calculated another index BDIWN as the difference in 100 m temperature anomalies between Box–W and Box–N from Argo observations and IOM. All the time series were calculated for September (0)–February (1) for every year and shown in Fig. 12e. The high correlation

Table 2 Positive, negative, and normal year with respect to Bay of Bengal Dipole

PBDI	NBDI	Normal year
1991, 1992, 1994, 1997, 2004, 2006, 2015	1996, 1998, 2000, 2005, 2010, 2012, 2013, 2014	1993, 1995, 1999, 2001, 2002, 2003, 2007, 2008, 2009, 2011

(0.81) between BDI and BDIWN from IOM indicated similarities in the characteristics of Box-N and Box-E. The correlation (0.77) between BDIWNs obtained distinctly from IOM and Argos during 2005–2015 implied the existence of dipole in the real ocean. It was observed that the correlations of BDI with DMI and Niño3.4 index were 0.58 and 0.63, respectively. Therefore, the BDI could be the possible indicator of IOD and ENSO events in the BoB. Also, there was a 1-month lag between BDI and IOD with lag correlation 0.64, but there was no lag between ENSO and BDI. When the value of BDI is greater (less) than 1 standrad deviation of BDI, the corresponding year is denoted as positive (negative) BDI year (Fig. 12e). The list of the PBDI and NBDI is listed in Table 2.

During the positive (negative) phases of BDI, the eastern BoB became cooler (warmer). To find the relationship of BDI with cyclone, we compared the index with the frequency of cyclonic disturbances (Fig. 12f). A close relationship was obtained; during the positive (negative) phases, the number of cyclonic disturbances was decreased (increased) possibly due to the change in the ocean heat content (Girishkumar and Ravichandran 2012). However, the cyclone is an ocean-atmosphere couple phenomenon, more detailed study with atmospheric processes will be carried out in the near future. The Chl-a concentration during OND was analyzed during positive and negative events of BDI. During PBDI, the negative anomalies in Chl-a were observed on the western BoB (Fig. 12g), due to the deepening of the thermocline (Fig. 10a, c). The dRWs were stronger during these events due to the favorable easterlies. During the NBDI events, the positive Chl-a anomalies on the western BoB (Fig. 12h) were noticed due to shallower thermocline and upwelling favorable winds (Fig. 10b, d). The analysis effectively suggested the impact of BoB dipole event on the primary productivity of the western of BoB.

5 Conclusions

This study deals with the interannual variability of equatorial and local forcing and its impact on the SSHA and thermocline during the IOD and ENSO events. Two model experiments were configured, one for whole IO and second for the BoB with climatological boundary conditions to prevent the interannual variations of the equatorial remote forcing for the period 1991–2015. The simulated ocean currents for IOM at the equator showed high correlation and skill score and indicated the capability of the model to reproduce the interannual features of the well-known Wyrtki jet. The seasonal surface currents and temperature comparisons also suggested the usability of the IOM for further studies for the BoB region. The spatial distribution of the first mode of the EOF (EOF1) of the IOM simulated SSHA matched reasonably well with AVISO. However, the BoBM did not show proper variation in SSHA, which indicated that the equatorial forcing played a dominant role on interannual variations of SSHA in the BoB through the coastally trapped KWs. The time series of the first principal component (PC1) showed good agreement with the same of the zonal wind stress at the equator, DMI and Nino 3.4 index, which confirmed the response of the SSHA to the equatorial forcing. The spatial distribution and time series of the PC1 showed the large variations in BoB in the OND during after the active phase of 2nd dKWs in OND in the BoB. The 2nd dKWs were stronger during NIOD and LN due to the stronger westerlies at the equator. The 2nd dKWs were weak during PIOD and EN, whereas the dRWs were comparatively stronger.

During the positive phases of IOD and ENSO, the eastern BoB showed a colder anomaly from 30 to 150 m depth due to weaker 2nd dKWs. Along the western side of BoB, a positive temperature anomaly and deeper D23 were observed due to the presence of a weaker cyclonic eddy on the south-western BoB, negative wind stress curl anomalies and stronger dRWs. Similarly, during the negative phases, the 2nd dKWs were stronger to make the eastern BoB warmer. The southward EICC on the western BoB was stronger leading to an intensified cyclonic eddy on the south-western BoB and shallow D23, which resulted in colder temperature anomalies. Additionally, positive wind stress curl anomalies made this region more upwelling favorable. A west-east dipole structure in subsurface temperature anomalies with the core around 100 m depth was noticed from IOM, which is also supported in the Argo observations and other reanalysis products. The dipole index (west-east) was calculated at 100 m temperature, which had a good correlation with the DMI. Therefore, this index could be useful to measure the impact of the IOD and ENSO in the BoB. During the positive (negative) phases of the BDI, the number of cyclonic disturbances was decreased (increased) over the BoB. Moreover, during PBDI (NBDI), the negative (positive) anomalies in Chl-a were observed on the western BoB, due to the deeper (shallower) thermocline, which can be a possible indicator of the primary productivity.

However, the usefulness of this new index will be analyzed in more details in our future work. We will also investigate the impact of subsurface temperature variability on Indian monsoon. Prior to this, salinity stratification is a very important phenomenon in the BoB. Therefore, the IOM simulations are to be used to study the salinity stratification and its impact on various ocean processes.

Acknowledgments Authors thank the Earth System Science Organization (ESSO)–Indian National Centre for Oceanic Information Services (INCOIS) for providing TropFlux datasets freely. Authors also thank the other data providers as mentioned in Sect. 2.2. Authors are thankful the anonymous reviewer and the editor for valuable suggestions. Authors also acknowledge Kiranmayi L for helping on the statistical methods used in the study. All figures are prepared using MATLAB.

Funding information Financial supports are from Space Application Centre (SAC), Indian Space Research Organization (Grant No. SAC/EPSA/4.19/2016) Science and Engineering Research Board (SERB, Grant No. SB/S4/AS-155/2014).

References

Ali MM, Singh N, Kumar M, Zheng Y, Bourassa M, Kishtawal C, Rao C (2018) Dominant modes of Upper Ocean heat content in the North Indian Ocean. Climate 6:71. https://doi.org/10.3390/cli6030071

Aparna SG, McCreary JP, Shankar D, Vinayachandran PN (2012) Signatures of Indian Ocean dipole and El Niño-Southern Oscillation events in sea level variations in the Bay of Bengal. J Geophys Res 117:C10012. https://doi.org/10.1029/2012JC008055

Argo (2019) Argo float data and metadata from global data assembly Centre (Argo GDAC). SEANOE. https://doi.org/10.17882/42182

Babu MT, Sarma YVB, Murty VSN, Vethamony P (2003) On the circulation in the Bay of Bengal during Northern spring inter-monsoon (March-April 1987). Deep Res Part II Top Stud Oceanogr 50:855–865. https://doi.org/10.1016/S0967-0645(02)00609-4

Balaguru K, Taraphdar S, Leung LR, Foltz GR (2014) Increase in the intensity of postmonsoon bay of Bengal tropical cyclones. Geophys Res Lett 41:3594–3601. https://doi.org/10.1002/2014GL060197

Balmaseda MA, Mogensen K, Weaver AT (2013) Evaluation of the ECMWF Ocean reanalysis system ORAS4. Q J R Meteorol Soc 139:1132–1161. https://doi.org/10.1002/qj.2063

Bonjean F, Lagerloef GSE (2002) Diagnostic model and analysis of the surface currents in the tropical Pacific Ocean. J Phys Oceanogr 32: 2938–2954. https://doi.org/10.1175/1520-0485(2002)032<2938:DMAAOT>2.0.CO;2

Carton JA, Giese BS (2008) A reanalysis of ocean climate using simple ocean data assimilation (SODA). Mon Weather Rev 136:2999–3017. https://doi.org/10.1175/2007MWR1978.1

Chacko N (2017) Chlorophyll bloom in response to tropical cyclone Hudhud in the Bay of Bengal: bio-Argo subsurface observations. Deep Res Part I Oceanogr Res Pap 124:66–72. https://doi.org/10.1016/j.dsr.2017.04.010

Chakravorty S, Gnanaseelan C, Chowdary JS, Luo J-J (2014) Relative role of El Niño and IOD forcing on the southern tropical Indian Ocean Rossby waves. J Geophys Res Ocean 119:5105–5122. https://doi.org/10.1002/2013JC009713

Chatterjee A, Shankar D, McCreary JP, Vinayachandran PN, Mukherjee A (2017) Dynamics of Andaman Sea circulation and its role in connecting the equatorial Indian Ocean to the bay of Bengal. J Geophys Res Ocean 122:3200–3218. https://doi.org/10.1002/2016JC012300

Chen G, Han W, Li Y, Wang D, McPhaden MJ (2015) Seasonal-to-interannual time-scale dynamics of the equatorial undercurrent in the Indian Ocean. J Phys Oceanogr 45:1532–1553. https://doi.org/10.1175/JPO-D-14-0225.1

Chen G, Han W, Shu Y, Li Y, Wang D, Xie Q (2016) The role of equatorial undercurrent in sustaining the eastern Indian Ocean upwelling. Geophys Res Lett 43:6444–6451. https://doi.org/10.1002/2016GL069433

Chen G, Li Y, Xie Q, Wang D (2018) Origins of Eddy kinetic energy in the bay of Bengal. J Geophys Res Ocean 123:2097–2115. https://doi.org/10.1002/2017JC013455

Chen G, Wang D, Hou Y (2012) The features and interannual variability mechanism of mesoscale eddies in the bay of Bengal. Cont Shelf Res 47:178–185. https://doi.org/10.1016/j.csr.2012.07.011

Cheng X, McCreary JP, Qiu B, Qi Y, Du Y, Chen X (2018) Dynamics of eddy generation in the central Bay of Bengal. J Geophys Res Ocean: 1–15. https://doi.org/10.1029/2018JC014100

Chowdary JS, Gnanaseelan C (2007) Basin-wide warming of the Indian Ocean during El Niño and Indian Ocean dipole years. Int J Climatol 27:1421–1438. https://doi.org/10.1002/joc.1482

Currie JC, Lengaigne M, Vialard J, Kaplan DM, Aumont O, Naqvi SWA, Maury O (2013) Indian Ocean dipole and El Niño/southern oscillation impacts on region al chlorophyll anomalies in the Indian Ocean. Biogeosciences 10:6677–6698

Dai A (2016) Historical and future changes in streamflow and continental runoff: a review. Terr Water Cycle Clim Chang Nat Human-Induced Impacts 17–37. https://doi.org/10.1002/9781118971772.ch2

Dandapat S, Chakraborty A, Kuttippurath J (2018) Interannual variability and characteristics of the East India coastal current associated with Indian Ocean dipole events using a high resolution regional ocean model. Ocean Dyn 68:1321–1334. https://doi.org/10.1007/s10236-018-1201-5

Devi KN, Sarangi RK (2017) Time-series analysis of chlorophyll-a, sea surface temperature, and sea surface height anomalies during 2003–2014 with special reference to EL niño, la niña, and indian ocean dipole (IOD) years. Int J Remote Sens 38:5626–5639. https://doi.org/10.1080/01431161.2017.1343511

Dey D, Sil S, Jana S, Pramanik S, Pandey PC (2017) An assessment of TropFlux and NCEP air-sea fluxes on ROMS simulations over the bay of Bengal region. Dyn Atmos Oceans 80:47–61. https://doi.org/10.1016/j.dynatmoce.2017.09.002

Durand F, Shankar D, Birol F, Shenoi SSC (2009) Spatiotemporal structure of the East India coastal current from satellite altimetry. J Geophys Res 114:C02013. https://doi.org/10.1029/2008JC004807

Fournier S, Vialard J, Lengaigne M, Lee T, Gierach MM, Chaitanya AVS (2017) Modulation of the Ganges-Brahmaputra River plume by the Indian Ocean dipole and eddies inferred from satellite observations. J Geophys Res Ocean 122:9591–9604. https://doi.org/10.1002/2017JC013333

Gangopadhyay A, Bharat Raj GN, Chaudhuri AH, Babu MT, Sengupta D (2013) On the nature of meandering of the springtime western boundary current in the bay of Bengal. Geophys Res Lett 40: 2188–2193. https://doi.org/10.1002/grl.50412

Girishkumar MS, Joseph J, Thangaprakash VP, Pottapinjara V, McPhaden MJ (2017) Mixed layer temperature budget for the northward propagating summer monsoon Intraseasonal oscillation (MISO) in the Central Bay of Bengal. J Geophys Res Ocean 122: 8841–8854. https://doi.org/10.1002/2017JC013073

Girishkumar MS, Ravichandran M (2012) The influences of ENSO on tropical cyclone activity in the bay of Bengal during October–December. J Geophys Res 117:C02033. https://doi.org/10.1029/2011JC007417

Girishkumar MS, Ravichandran M, Han W (2013) Observed intraseasonal thermocline variability in the bay of Bengal. J Geophys Res Ocean 118:3336–3349. https://doi.org/10.1002/jgrc.20245

Girishkumar MS, Ravichandran M, McPhaden MJ, Rao RR (2011) Intraseasonal variability in barrier layer thickness in the south central bay of Bengal. J Geophys Res 116:C03009. https://doi.org/10.1029/2010JC006657

Girishkumar MS, Suprit K, Chiranjivi J, Udya Bhaskar TVS, Ravichandran M, Shesu RV, Pattabhi Rama Rao E (2014) Observed oceanic response to tropical cyclone Jal from a moored buoy in the south-western bay of Bengal. Ocean Dyn 64:325–335. https://doi.org/10.1007/s10236-014-0689-6

Gnanaseelan C, Vaid BH, Polito PS (2008) Impact of biannual rossby waves on the indian ocean dipole. IEEE Geosci Remote Sens Lett 5: 427–429. https://doi.org/10.1109/LGRS.2008.919505

Gnanaseelan C, Deshpande A, McPhaden MJ (2012) Impact of Indian Ocean dipole and El Niño/southern oscillation wind-forcing on the Wyrtki jets. J Geophys Res 117:C08005. https://doi.org/10.1029/2012JC007918

Gordon AL, Shroyer EL, Mahadevan A, Sengupta D, Freilich M (2016) Bay of Bengal: 2013 northeast monsoon upper-ocean circulation. Oceanography 29:82–91. https://doi.org/10.5670/oceanog.2016.41

Haidvogel DB, Arango H, Budgell WP, Cornuelle BD, Curchitser E, Di Lorenzo E, Fennel K, Geyer WR, Hermann AJ, Lanerolle L, Levin J, McWilliams JC, Miller AJ, Moore AM, Powell TM, Shchepetkin AF, Sherwood CR, Signell RP, Warner JC, Wilkin J (2008) Ocean forecasting in terrain-following coordinates: formulation and skill assessment of the Regional Ocean modeling system. J Comput Phys 227:3595–3624. https://doi.org/10.1016/j.jcp.2007.06.016

Haidvogel DB, Arango HG, Hedstrom K, Beckmann A, Malanotte-Rizzoli P, Shchepetkin AF (2000) Model evaluation experiments in the North Atlantic Basin: simulations in nonlinear terrain-following coordinates. Dyn Atmos Oceans 32:239–281. https://doi.org/10.1016/S0377-0265(00)00049-X

Iskandar I, Masumoto Y, Mizuno K (2009) Subsurface equatorial zonal current in the eastern Indian Ocean. J Geophys Res 114:C06005. https://doi.org/10.1029/2008JC005188

Jana S, Gangopadhyay A, Chakraborty A (2015) Impact of seasonal river input on the bay of Bengal simulation. Cont Shelf Res 104:45–62. https://doi.org/10.1016/j.csr.2015.05.001

Jana S, Gangopadhyay A, Lermusiaux PFJ, Chakraborty A, Sil S, Haley PJ (2018) Sensitivity of the bay of Bengal upper ocean to di ff erent winds and river input conditions. J Mar Syst 187:206–222. https://doi.org/10.1016/j.jmarsys.2018.08.001

Jongaramrungruang S, Seo H, Ummenhofer CC (2017) Intraseasonal rainfall variability in the bay of Bengal during the summer monsoon: coupling with the ocean and modulation by the Indian Ocean dipole. Atmos Sci Lett 18:88–95. https://doi.org/10.1002/asl.729

Krishnamurti TN, Jana S, Krishnamurti R, Kumar V, Deepa R, Papa F, Bourassa MA, Ali MM (2017) Monsoonal intraseasonal oscillations in the ocean heat content over the surface layers of the bay of Bengal. J Mar Syst 167:19–32. https://doi.org/10.1016/j.jmarsys.2016.11.002

Kumar BP, Vialard J, Lengaigne M, Murty VSN, McPhaden MJ (2012) TropFlux: air-sea fluxes for the global tropical oceans-description and evaluation. Clim Dyn 38:1521–1543. https://doi.org/10.1007/s00382-011-1115-0

Kumari A, Kumar SP, Chakraborty A (2017) Seasonal and interannual variability in the barrier layer of the bay of Bengal. J Geophys Res Ocean 123:1001–1015. https://doi.org/10.1002/2017JC013213

Large WG, McWilliams JC, Doney SC (1994) Oceanic vertical mixing _ a review and a model with a nonlocal boundary layer parameterization.pdf. Rev Geophys:363–403. https://doi.org/10.1029/94RG01872

Li Y, Han W, Hu A, Meehl GA, Wang F (2018) Multidecadal changes of the upper Indian Ocean heat content during 1965-2016. J Clim 31:7863–7884. https://doi.org/10.1175/JCLI-D-18-0116.1

Li J, Liang C, Tang Y, Liu X, Lian T, Shen Z, Li X (2017) Impacts of the IOD-associated temperature and salinity anomalies on the intermittent equatorial undercurrent anomalies. Clim Dyn 51:1391–1409. https://doi.org/10.1007/s00382-017-3961-x

Mandal S, Sil S, Gangopadhyay A, Murty T, Swain D (2018) On extracting high-frequency tidal variability from HF radar data in the northwestern bay of Bengal. J Oper Oceanogr 8778:1–17. https://doi.org/10.1080/1755876X.2018.1479571

Masumoto Y, Hase H, Kuroda Y, Matsuura H, Takeuchi K (2005) Intraseasonal variability in the upper layer currents observed in the eastern equatorial Indian Ocean. Geophys Res Lett 32:1–4. https://doi.org/10.1029/2004GL021896

McCreary JP (1981) A linear stratified ocean model of the coastal undercurrent. Philos Trans R Soc Lond 298:603–635. https://doi.org/10.1098/rsta.1981.0176

McCreary JP (1985) Modeling equatorial ocean circulation. Annu Rev Fluid Mech 17:359–409. https://doi.org/10.1146/annurev.fl.17.010185.002043

McCreary JP, Kundu PK, Molinari RL (1993) A numerical investigation of dynamics, thermodynamics and mixed-layer processes in the Indian Ocean. Prog Oceanogr 31:181–244

Mukherjee A, Kalita BK (2019) Signature of La Niña in interannual variations of the East India coastal current during spring. Clim Dyn 53:1–18. https://doi.org/10.1007/s00382-018-4601-9

Neelin JD, Battisti DS, Hirst AC, Jin FF, Wakata Y, Yamagata T, Zebiak SE (1998) ENSO theory. J Geophys Res Ocean 103:14261–14290. https://doi.org/10.1029/97JC03424

Nienhaus MJ, Subrahmanyam B, Murty VSN (2012) Altimetric observations and model simulations of coastal kelvin waves in the bay of Bengal. Mar Geod 35:190–216. https://doi.org/10.1080/01490419.2012.718607

Nyadjro ES, McPhaden MJ (2014) Variability of zonal currents in the eastern equatorial Indian Ocean on seasonal to interannual time scales. J Geophys Res Ocean 119:7969–7986. https://doi.org/10.1002/2014JC010380

Penven P, Debreu L, Marchesiello P, McWilliams JC (2006) Evaluation and application of the ROMS 1-way embedding procedure to the Central California upwelling system. Ocean Model 12:157–187. https://doi.org/10.1016/j.ocemod.2005.05.002

Potemra JT, Luther ME, O'Brien JJ (1991) The seasonal circulation of the upper ocean in the bay of Bengal. J Geophys Res 96:12667. https://doi.org/10.1029/91JC01045

Prasanna Kumar S, Unnikrishnan AS (1995) Seasonal cycle of temperature and associated wave phenomenon in the upper layers of the bay of Bengal. J Geophys Res Ocean 100:13585–13593. https://doi.org/10.1029/95JC01037

Prerna S, Chatterjee A, Mukherjee A, Ravichandran M, Shenoi SS (2019) Wyrtki jets: role of intraseasonal forcing. J Earth Syst Sci 128(2019):21. https://doi.org/10.1007/s12040-018-1042-0

Rao RR, Girish Kumar MS, Ravichandran M, Rao AR, Gopalakrishna VV, Thadathil P (2010) Interannual variability of kelvin wave propagation in the wave guides of the equatorial Indian Ocean, the coastal bay of Bengal and the southeastern Arabian Sea during 1993-2006. Deep Res Part I Oceanogr Res Pap 57:1–13. https://doi.org/10.1016/j.dsr.2009.10.008

Rao SA, Behera SK (2005) Subsurface influence on SST in the tropical Indian Ocean: structure and interannual variability. Dyn Atmos Oceans 39:103–135. https://doi.org/10.1016/j.dynatmoce.2004.10.014

Reynolds RW, Smith TM, Liu C, Chelton DB, Casey KS, Schlax MG (2007) Daily high-resolution blended analyses for sea surface temperature. J Clim 20:5473–5496

Sachidanandan C, Lengaigne M, Muraleedharan PM, Mathew B (2017) Interannual variability of zonal currents in the equatorial Indian Ocean: respective control of IOD and ENSO. Ocean Dyn 67:857–873. https://doi.org/10.1007/s10236-017-1061-4

Saji NH, Goswami BN, Vinayachandran PN, Yamagata T (1999) A dipole mode in the tropical Indian Ocean. Nature 401:360–363. https://doi.org/10.1038/43854

Sayantani O, Gnanaseelan C (2015) Tropical Indian Ocean subsurface temperature variability and the forcing mechanisms. Clim Dyn 44(9–10):2447–2462. https://doi.org/10.1007/s00382-014-2379-y

Schott FA, McCreary JP (2001) The monsoon circulation of the Indian Ocean. Prog Oceanogr 51:1–123. https://doi.org/10.1016/S0079-6611(01)00083-0

Schott FA, Xie SP, McCreary JP (2009) Indian ocean circulation and climate variability. Rev Geophys 47. https://doi.org/10.1029/2007RG000245

Senan R, Sengupta D, Goswami BN (2003) Intraseasonal "monsoon jets" in the equatorial Indian Ocean. Geophys Res Lett 30:1–4. https://doi.org/10.1029/2003GL017583

Shankar D, McCreary JP, Han W, Shetye SR (1996) Dynamics of the East India Coastal Current: 1. Analytic solutions forced by interior

Ekman pumping and local alongshore winds. J Geophys Res 101: 13975. https://doi.org/10.1029/96JC00559

Sharma R, Agarwal N, Basu S, Agarwal VK (2007) Impact of satellite-derived Forcings on Numerical Ocean model simulations and study of sea surface salinity variations in the Indian Ocean. J Clim 20:871–890. https://doi.org/10.1175/JCLI4032.1

Shchepetkin AF, McWilliams JC (2003) A method for computing horizontal pressure-gradient force in an oceanic model with a non-aligned vertical coordinate. J Geophys Res 108:3090. https://doi.org/10.1029/2001JC001047

Shchepetkin AF, McWilliams JC (2005) The regional oceanic modeling system (ROMS): a split-explicit, free-surface, topography-following-coordinate oceanic model. Ocean Model 9:347–404. https://doi.org/10.1016/j.ocemod.2004.08.002

Shee A, Sil S, Gangopadhyay A, Gawarkiewicz G, Ravichandran M (2019) Seasonal evolution of oceanic upper layer processes in the northern bay of Bengal following a single Argo float. Geophys Res Lett 46:5369–5377. https://doi.org/10.1029/2019GL082078

Sherin VR, Durand F, Gopalkrishna VV, Anuvinda S, Chaitanya AVS, Bourdallé-Badie R, Papa F (2018) Signature of Indian Ocean dipole on the western boundary current of the bay of Bengal. Deep Res Part I Oceanogr Res Pap 136:91–106. https://doi.org/10.1016/j.dsr.2018.04.002

Shetye SR, Gouveia AD, Shankar D, Shenoi SSC, Vinayachandran PN, Sundar D, Michael GS, Nampoothiri G (1996) Hydrography and circulation in the western bay of Bengal during the northeast monsoon. J Geophys Res Ocean 101:14011–14025. https://doi.org/10.1029/95JC03307

Shetye SR, Gouveia AD, Shenoi SSC, Sundar D, Michael GS, Nampoothiri G (1993) The Western boundary current of the seasonal subtropical gyre in the bay of Bengal. J Geophys Res 98:945–954. https://doi.org/10.1029/92JC02070

Siderius M, Porter MB, Hursky P, McDonald V (2007) Effects of ocean thermocline variability on noncoherent underwater acoustic communications. J Acoust Soc Am 121:1895–1908. https://doi.org/10.1121/1.2436630

Sil S, Chakraborty A (2011a) Simulation of East India coastal features and validation with satellite altimetry and Drifter Ocean and. Int J Ocean Clim Syst 2:279–289. https://doi.org/10.1260/1759-3131.2.4.279

Sil S, Chakraborty A (2011b) Numerical simulation of seasonal variations in circulations of the bay of Bengal. J Oceanogr Mar Sci 2:127–135

Sil S, Chakraborty A (2012) The mechanism of the 20 °C isotherm depth oscillations for the bay of Bengal the mechanism of the 20 °C isotherm depth oscillations for the bay of Bengal. https://doi.org/10.1080/01490419.2011.637865

Smith WH, Sandwell D (1997) Global Sea floor topography from satellite altimetry and ship depth soundings. Science (80-) 277:1956–1962. https://doi.org/10.1126/science.277.5334.1956

Somayajulu YK, Murty VSN, Sarma YVB (2003) Seasonal and interannual variability of surface circulation in the bay of Bengal from TOPEX/Poseidon altimetry. Deep Res II 50:867–880. https://doi.org/10.1016/S0967-0645(02)00610-0

Song Y, Haidvogel D (1994) A semi-implicit ocean circulation model using a generalized topography-following coordinate system. J Comput Phys 115:228–244. https://doi.org/10.1006/jcph.1994.1189

Sreenivas P, Gnanaseelan C, Prasad KVSR (2012) Influence of El Nino and Indian Ocean dipole on sea level variability in the bay of Bengal. Glob Planet Chang 80–81:215–225. https://doi.org/10.1016/j.gloplacha.2011.11.001

Strub PT, Corinne J (2015) Altimeter-derived seasonal circulation on the southwestAtlantic shelf: 278–438S. J Geophys Res Ocean 120:1–28. https://doi.org/10.1002/2015JC010769.Received

Taylor KE (2001) Summarizing multiple aspects of model performance in a single diagram. J Geophys Res 106:7183–7192. https://doi.org/10.1029/2000JD900719

Thadathil P, Gopalakrishna VV, Muraleedharan PM, Reddy GV, Araligidad N, Shenoy S (2002) Surface layer temperature inversion in the bay of Bengal. Deep Res Part I Oceanogr Res Pap 49:1801–1818. https://doi.org/10.1016/S0967-0637(02)00044-4

Vinayachandran P, Francis PA, Suryachandra Rao A (2009) Indian Ocean dipole: processes and impacts. Curr trends Sci:569–589

Vinayachandran PN, Iizuka S, Yamagata T (2002) Indian Ocean dipole mode events in an ocean general circulation model. Deep Res Part II Top Stud Oceanogr 49:1573–1596. https://doi.org/10.1016/S0967-0645(01)00157-6

Vinayachandran PN, Masumoto Y, Mikawa T, Yamagata T (1999) Intrusion of the southwest monsoon current into the bay of Bengal. J Geophys Res Ocean 104:11077–11085. https://doi.org/10.1029/1999JC900035

Vinayachandran PN, Matthews AJ, Vijay Kumar K, Sanchez-Franks A, Thushara V, George J, Vijith V, Webber BGM, Queste BY, Roy R, Sarkar A, Baranowski DB, Bhat GS, Klingaman NP, Peatman SC, Parida C, Heywood KJ, Hall R, King B, Kent EC, Nayak AA, Neema CP, Amol P, Lotliker A, Kankonkar A, Gracias DG, Vernekar S, D.Souza AC, Valluvan G, Pargaonkar SM, Dinesh K, Giddings J, Joshi M (2018) BoBBLE (bay of Bengal boundary layer experiment): ocean–atmosphere interaction and its impact on the south Asian monsoon. Bull Am Meteorol Soc BAMS-D-16-0230.1. https://doi.org/10.1175/BAMS-D-16-0230.1

Webster PJ, Moore AM, Loschnigg JP, Leben RR (1999) Coupled ocean–atmosphere dynamics in the Indian Ocean during 1997–98. Nature 401:356–360. https://doi.org/10.1038/43848

Wong A, Keeley R, Carval T (2009) The Argo data management team, Argo data management, Version 2.5

Wyrtki K (1973) An equatorial jet in the Indian Ocean. Sci J 181(4096): 262–264

Yu L (2003) Variability of the depth of the 20°C isotherm along 6°N in the bay of Bengal: its response to remote and local forcing and its relation to satellite SSH variability. Deep Res Part II Top Stud Oceanogr 50:2285–2304. https://doi.org/10.1016/S0967-0645(03)00057-2

Yu L, O'Brien JJ, Yang J (1991) On the remote forcing of the circulation in the bay of Bengal. J Geophys Res 96:20449. https://doi.org/10.1029/91JC02424

Yu W, Xiang B, Liu L, Liu N (2005) Understanding the origins of interannual thermocline variations in the tropical Indian Ocean. Geophys Res Lett 32:1–4. https://doi.org/10.1029/2005GL024327